Liver type 1 innate lymphoid cells lacking IL-7 receptor are a native killer cell subset fostered by parenchymal niches

Takuma Asahi[1,2], Shinya Abe[1,2], Guangwei Cui[1], Akihiro Shimba[1,3], Tsukasa Nabekura[4,5,6], Hitoshi Miyachi[7], Satsuki Kitano[7], Keizo Ohira[1,8], Johannes M. Dijkstra[9], Masaki Miyazaki[10], Akira Shibuya[4,5,6], Hiroshi Ohno[11], and Koichi Ikuta[1,*]

[1]Laboratory of Immune Regulation, Department of Virus Research, Institute for Life and Medical Sciences, Kyoto University, Kyoto 606-8507, Japan; [2]Graduate School of Medicine, Kyoto University, Kyoto 606-8501, Japan; [3]Department of Human Health Sciences, Graduate School of Medicine, Kyoto University, Kyoto 606-8507, Japan; [4]Life Science Center for Survival Dynamics, Tsukuba Advanced Research Alliance (TARA), University of Tsukuba, 1-1-1 Tennodai, Tsukuba, Ibaraki 305-8575, Japan; [5]Department of Immunology, Faculty of Medicine, University of Tsukuba, 1-1-1 Tennodai, Tsukuba, Ibaraki 305-8575, Japan; [6]R&D Center for Innovative Drug Discovery, University of Tsukuba, 1-1-1 Tennodai, Tsukuba, Ibaraki 305-8575, Japan; [7]Reproductive Engineering Team, Institute for Life and Medical Sciences, Kyoto University, Kyoto 606-8507, Japan; [8]Graduate School of Biostudies, Kyoto University, Kyoto 606-8501, Japan; [9]Center for Medical Science, Fujita Health University, Aichi 470-1192, Japan; [10]Laboratory of Immunology, Institute for Life and Medical Sciences, Kyoto University, Kyoto 606-8507, Japan; [11]Laboratory for Intestinal Ecosystem, RIKEN Center for Integrative Medical Sciences (IMS), Yokohama 230-0045, Japan

*Correspondence
E-mail address: ikuta.koichi.6c@kyoto-u.ac.jp
Laboratory of Immune Regulation, Department of Virus Research, Institute for Life and Medical Sciences, Kyoto University, Kyoto 606-8507, Japan
Tel, +81-75-751-4012; Fax, +81-75-751-4810.

Keywords: ILC1s; NK cells; Interleukin 15; development; niche; cytotoxicity

Abstract 191 words

Group 1 innate lymphoid cells (G1-ILCs), including circulating natural killer (NK) cells and tissue-resident type 1 ILCs (ILC1s), are innate immune sentinels critical for responses against infection and cancer. In contrast to relatively uniform NK cells through the body, diverse ILC1 subsets have been characterized across and within tissues in mice, but their developmental and functional heterogeneity remain unsolved. Here, using multimodal *in vivo* approaches including fate-mapping and targeting of the interleukin 15 (IL-15)-producing microenvironment, we demonstrate that liver parenchymal niches support the development of a cytotoxic ILC1 subset lacking IL-7 receptor ($7R^-$ ILC1s). During ontogeny, fetal liver (FL) G1-ILCs arise perivascularly and then differentiate into $7R^-$ ILC1s within sinusoids. Hepatocyte-derived IL-15 supports parenchymal development of FL G1-ILCs to maintain adult pool of $7R^-$ ILC1s. IL-$7R^+$ ($7R^+$) ILC1s in the liver, candidate precursors for $7R^-$ ILC1s, are not essential for $7R^-$ ILC1 development in physiological conditions. Functionally, $7R^-$ ILC1s exhibit killing activity at steady state through granzyme B expression, which is underpinned by constitutive mTOR activity, unlike NK cells with exogenous stimulation-dependent cytotoxicity. Our study reveals the unique ontogeny and functions of liver-specific ILC1s, providing a detailed interpretation of ILC1 heterogeneity.

Introduction

Group 1 innate lymphoid cells (G1-ILCs) are innate immune cells contributing to surveillance of intracellular infections and tumors. G1-ILCs comprise two subtypes: natural killer (NK) cells and type 1 ILCs (ILC1s), that share fundamental features such as NK1.1^{+}NKp46^{+} phenotype, expression of T-bet, and IFN-γ production (Jacquelot et al., 2022; Stokic-Trtica et al., 2020; Vivier et al., 2018). In contrast, mouse ILC1s can be distinguished from NK cells by their CD49a^{+}CD49b^{-} phenotype, strict tissue-residency, and Eomes-independence (Daussy et al., 2014; Gasteiger et al., 2015; Peng et al., 2013; Sojka et al., 2014). In addition, developmental paths of ILC1s are basically distinct from NK cells, as confirmed by the identification of non-NK common ILC progenitors (ILCPs) expressing PLZF and/or PD-1 (Constantinides et al., 2015; Constantinides et al., 2014; Yu et al., 2016) and liver-resident Lin^{-}Sca-1^{+}Mac-1^{+} (LSM) and Lin^{-}CD49a^{+}CD122^{+} ILC1 precursors (Bai et al., 2021).

Functional differences between NK cells and ILC1s have also been recognized, though some confusion remains, particularly in cytotoxicity. In mice, NK cells are traditionally considered as more cytotoxic than ILC1s (Vivier et al., 2018), though this view has been questioned recently (Dadi et al., 2016; Kansler et al., 2022; Krabbendam et al., 2021; Nixon et al., 2022; Yomogida et al., 2021). Indeed, murine NK cells show low expression of cytotoxic molecules and only minimal cytotoxicity in their steady state (Fehniger et al., 2007). The cytotoxicity of NK cells requires the mTOR-dependent metabolic reprogramming mediated by cytokine signaling such as IL-15 or by NK receptor engagement (Marçais et al., 2014; Nandagopal et al., 2014), but whether such cytotoxic machinery also exists in ILC1s is unclear. By contrast, ILC1s can immediately respond and produce IFN-γ during liver injury (Nabekura et al., 2020) and virus infection (Weizman et al., 2017), highlighting the unique roles of ILC1s in the ignition of type 1 immunity in tissues. Thus, examining the development, function, and heterogeneity of ILC1s could lead to further understanding of local immune regulation and novel therapeutic strategies.

Recent high-resolution analysis has uncovered ILC1 heterogeneity and development. Liver ILC1s are separated into IL-7R-negative (7R^{-}) and -positive (7R^{+}) subsets (Friedrich et al., 2021; Sparano et al., 2022; Yomogida et al., 2021). G1-ILCs in the fetal liver (FL) are identified as precursors of ILC1s (Chen et al., 2022; Sparano et al., 2022), especially of Ly-49E^{+} ILC1s that are included in 7R^{-} ILC1s (Chen et al., 2022). In addition, 7R^{+} ILC1s in the liver, salivary glands (SG), and small intestines can give rise to 7R^{-} ILC1s in response to cytokines and inflammations (Friedrich et al., 2021), suggesting that 7R^{+} ILC1s are also

potential precursors for 7R$^-$ ILC1s. However, several reports have suggested different models. In ILC1-related inflammation models reported so far, including contact hypersensitivity, MCMV infection, and liver injury, ILC1s with high cytokine receptors (IL-7R, IL-18R, and/or CD25) are induced and accumulate in the liver (Nabekura et al., 2020; Wang et al., 2018; Weizman et al., 2019). Furthermore, an organ-wide single cell RNA sequencing (scRNA-seq) analysis reveals that liver 7R$^-$ ILC1s represent a unique population distinct from SG and small intestines (McFarland et al., 2021), suggesting the absence of universal differentiation programs of ILC1s conserved across tissues. Thus, concepts of ILC1 heterogeneity and development are still controversial.

Additionally, environmental factors regulating ILC1 development are poorly understood. Accumulating evidence has shown that development and maintenance of ILCs are strictly associated with their resident tissue microenvironment, called niche (Ikuta et al., 2021; McFarland and Colonna, 2020; Murphy et al., 2022). G1-ILC homeostasis heavily depends on interleukin 15 (IL-15), that is transpresented from hematopoietic and stromal cells as an IL-15/IL-15Rα complex to locally promote the development, survival, and proliferation of memory CD8 T cells, NKT cells, and G1-ILCs in various tissues (Ikuta et al., 2021; Klose et al., 2014; Lodolce et al., 1998). However, how tissue environment regulates ILC1 homeostasis and whether specific niches control the formation of ILC1 heterogeneity are yet to be characterized.

Based on fate-mapping, transfer studies, and targeting of the IL-15-producing microenvironment, we have addressed the developmental processes of heterogenous ILC1 subsets. Adult liver (AL) 7R$^+$ ILC1s are not converted to 7R$^-$ ILC1s *in vivo* and RORα deficiency results in selective reduction of 7R$^+$ ILC1s, suggesting that 7R$^+$ ILC1s are not necessary for the development of 7R$^-$ ILC1s. FL G1-ILCs originate from perivascular sites of the liver and then infiltrate into sinusoids to give rise to AL 7R$^-$ ILC1s. Hepatocyte-derived IL-15 supports FL G1-ILCs development in parenchyma, thereby maintaining mature 7R$^-$ ILC1s in sinusoids. Functionally, 7R$^-$ ILC1s exert inflammation-independent cytotoxicity through granzyme B expression, which is underpinned by their tonic mTOR activity. Our findings reveal that 7R$^-$ ILC1s represent an ILC subset with unique developmental processes and unconventional native cytotoxicity distinct from NK cells and 7R$^+$ ILC1s.

Results

Fetal and adult liver contain *bona fide* ILC1s lacking IL-7R

To characterize and make the relationships among fetal and adult G1-ILCs clear, we first assessed their expression of NK- and ILC-signature molecules. FL G1-ILCs, adult tissue ILC1s, and NK cells were identified as CD49a^{+}CD49b^{int}, CD49a^{+}CD49b^{lo}, and CD49a^{-}CD49b^{+} populations within G1-ILCs, respectively (Figure 1A). FL G1-ILCs highly expressed CXCR6, TRAIL, and CD200R, resembling adult tissue ILC1s, though they completely lacked IL-7R expression (Figure 1B and 1C). AL contains both IL-7R-negative (7R^{-}) and -positive (7R^{+}) ILC1s (Figure 1C), as reported previously (Friedrich et al., 2021; Sparano et al., 2022; Yomogida et al., 2021). In contrast, CD49a^{+}CD49b^{lo} ILC1s in bone marrow (BM), corresponding to previously reported immature ILC1s (iILC1s) that have ability to give rise to liver ILC1s (Klose et al., 2014), were mostly IL-7R^{+}, similar to other tissues including the spleen, mesenteric lymph nodes, peritoneal cavity, and small intestines (Figure 1C and 1D). Despite the differential IL-7R expression, the frequencies and numbers of AL 7R^{-} and 7R^{+} ILC1s were not reduced in IL-7$^{-/-}$ mice (Figure 1–figure supplement 1A and 1B), consistent with the basic property of G1-ILCs of being IL-7-independent (Klose et al., 2014; Robinette et al., 2017).

We further assessed the relevance among G1-ILC subsets by bulk RNA sequencing (RNA-seq). All analyzed G1-ILC populations expressed *Tbx21* (T-bet) but not *Rorc* (RORγt), suggesting the lack of ILC3 contamination (Figure 1–figure supplement 1C). Consistent with surface phenotype, FL G1-ILCs and AL 7R^{-} ILC1s as well as BM iILC1s and AL 7R^{+} ILC1s shared high expression of ILC1 signature genes (*P2rx7*, *Zfp683*, and *Cd3g*) and low expression of NK cell signature genes (*Sell*, *Klra4*, and *Klra8*) (Figure 1E). By contrast, 7R^{+} ILC1s and BM iILC1s showed higher expression of genes related to cytokine responses (*Il7r*, *Il2ra*, *Icos*, and *Kit*) compared to other G1-ILC subsets (Figure 1–figure supplement 1D). Conversely, FL G1-ILCs and 7R^{-} ILC1s poorly expressed cytokine receptor-related genes (*Il7r*, *Il18r1*, and *Il18rap*) (Figure 1E) and exhibited less cytokine-responsive characters (Figure 1–figure supplement 1E). Although FL G1-ILCs were unique in terms of their high proliferative status (Figure 1–figure supplement 1F and 1G), principal component analysis (PCA) revealed that the overall transcriptional state of FL G1-ILCs was close to 7R^{-} ILC1s (Figure 1F). 7R^{+} ILC1s located rather close to BM iILC1s in PCA, suggesting their cross-tissue similarity. These results show the transcriptional resemblance between FL G1-ILCs and AL 7R^{-} ILC1s or between BM iILC1s and AL 7R^{+} ILC1s.

Given the ILC1-like transcriptional programs and T-bet^{+}Eomes^{-} phenotype of FL G1-ILCs and AL 7R^{-} ILC1s (Figure 1G), they were considered as ILC1s but not NK cells. To precisely verify their lineage, we performed fate-mapping of ILCPs by using PLZF-GFP-Cre Rosa26-YFP reporter (PLZF-fm) mice (Constantinides et al., 2014). In these mice, ILCP progenies including ILC1s, ILC2s, and ILC3s but not LTi or NK cells are preferentially labeled by YFP, though a certain ratio of blood cells expresses YFP due to the pre-hematopoietic PLZF expression (Constantinides et al., 2014). To remove this background YFP labelling, we used chimeric mice reconstituted with YFP^{-}Lin^{-}Sca1^{+}c-Kit^{+} (LSK) cells sorted from BM of PLZF-fm mice. In the chimeric mice, AL 7R^{-} and 7R^{+} ILC1s as well as other adult tissue ILC1s prominently expressed YFP (Figure 1H and 1I). A similar trend was observed when using straight PLZF-fm mice or chimeric mice reconstituted with FL LSK cells from PLZF-fm mice (Figure 1–figure supplement 1H and 1I). Furthermore, FL G1-ILCs mostly expressed YFP in straight PLZF-fm mice (Figure 1J), in line with a previous fate-mapping study of neonatal liver G1-ILCs (Constantinides et al., 2015). Thus, these results indicate that *bona fide* ILC1s lacking IL-7R are enriched in FL and AL.

7R^{+} ILC1s minimally contribute to the development of 7R^{-} ILC1s

A previous study reported that 7R^{+} ILC1s behaved as the precursors of 7R^{-} ILC1s when cultured *in vitro* or transferred into lymphopenic mice (Friedrich et al., 2021). However, in the liver, while 7R^{+} ILC1s were nearly absent in infants and accumulated with age, 7R^{-} ILC1s were predominant in young mice, decreased with age, and eventually depleted (Figure 2A–2C). These observations suggest that the development and maintenance of 7R^{-} ILC1s are independent from 7R^{+} ILC1s in physiological conditions.

To test this hypothesis, we first explored whether there were molecular pathways controlling the development of each ILC1 population individually. RNA-seq revealed that 7R^{+} ILC1s highly expressed RORα and were positively enriched with gene sets “RORA activates gene expression” relative to 7R^{-} ILC1s, based on gene set enrichment analysis (GSEA) (Figure 2D). We therefore generated RORα$^{-/-}$ mice to test the effect of RORα for 7R^{+} ILC1s. As RORα$^{-/-}$ mice tend to die within four weeks after birth, we analyzed adult RORα$^{+/-}$ mice or two weeks old RORα$^{-/-}$ mice. 7R^{+} ILC1s were significantly reduced in RORα$^{+/-}$ mice, while NK cells and 7R^{-} ILC1s were unchanged (Figure 2E). In RORα$^{-/-}$ mice, though whole ILC1s were significantly reduced as reported recently (Song et al., 2021), 7R^{+} ILC1s were the subset most apparently affected (Figure 2F). These data suggest that the

development of 7R$^-$ ILC1s do not significantly depend on the presence of 7R$^+$ ILC1s.

To make the developmental relationships between 7R$^-$ and 7R$^+$ ILC1s clearer, we conducted adoptive transfer experiments under physiological conditions by using unirradiated CD45.1 WT host mice. 7R$^-$ and 7R$^+$ ILC1s were isolated from AL, transferred, and the host liver were analyzed. For at least 2 months, little conversion was observed between 7R$^-$ and 7R$^+$ ILC1s (Figure 2G–I). In addition, transferred BM iILC1s gave rise to AL 7R$^+$ ILC1s but not to 7R$^-$ ILC1s (Figure 2–figure supplement 1A and 1B), consistent with their transcriptional resemblance. However, parabiosis experiments showed that the replacement rate of AL 7R$^+$ ILC1s were low (<5%), though significantly higher than that of 7R$^-$ ILC1s (Figure 2–figure supplement 1C), suggesting that both ILC1 subsets are tissue-resident. Thus, whether BM iILC1s actually contribute to AL 7R$^+$ ILC1 pool is still unclear. To test the phenotypical stability of ILC1s in inflammatory states, we injected IL-15/IL-15Rα complex repeatedly into host mice that had received CPD-labeled 7R$^-$ and 7R$^+$ ILC1s. NK cells and 7R$^+$ ILC1s proliferated more than 7R$^-$ ILC1s after the stimulation (Figure 2J), consistent with their basal Ki-67 expression levels (Figure 1–figure supplement 1G) and properties of cytokine responsiveness (Figure 1–figure supplement 1E). 7R$^-$ and 7R$^+$ ILC1s were stable even after the IL-15/IL-15Rα stimulation (Figure 2K), confirming their stability in activated states. These results show that 7R$^+$ ILC1s were rarely converted to 7R$^-$ ILC1s and not essential for the development of 7R$^-$ ILC1s under physiological conditions.

FL G1-ILCs arise at hepatic parenchyma and give rise to 7R$^-$ ILC1s in sinusoids

We next address the contribution of FL G1-ILCs to the development of AL 7R$^-$ ILC1s. Adoptively transferred FL G1-ILCs differentiated into CD49a$^+$CD49b^{lo} mature ILC1s in AL (Figure 3A) and they completely lacked IL-7R (Figure 3B). To confirm the direct contribution of FL G1-ILCs to the adult pool of 7R$^-$ ILC1s, we performed fate-mapping experiments using NKp46-CreERT2 mice (Nabekura and Lanier, 2016) crossed with Rosa26-tdTomato mice. After tamoxifen injection into pregnant mice at E17.5, liver of neonatal and 4 weeks old pups were analyzed. TdTomato expression was clearly restricted to IL-7R$^-$ fractions within neonatal G1-ILCs and AL ILC1s (Figure 3C–3E, Figure 3–figure supplement 1A), consistent with previous studies (Chen et al., 2022; Sparano et al., 2022). As shown in these studies, fate-mapped 7R$^-$ ILC1s showed a skewed expression of Ly49E/F, though they also contained Ly49E/F$^-$ population (20–25%) (Figure 3–figure supplement 1B–1D). Labeling efficiency was 40% in neonatal IL-7R$^-$ G1-ILCs and 20% in 7R$^-$ ILC1s in 4 weeks old mice (Figure 3F and 3G). These results confirm a direct, albeit partial, contribution of FL G1-ILCs to the adult

pool of $7R^-$ ILC1s.

To investigate the detailed developmental process of FL G1-ILCs and AL ILC1s *in vivo*, we examined their spatiotemporal distributions. In immunostaining analysis, FL G1-ILCs were identified as $NKp46^+$ cells in WT mice (Figure 4A). AL NK cells and ILC1s were identified as $NKp46^+GFP^-$ and $NKp46^+GFP^+$ cells in $CXCR6^{GFP/+}$ mice, respectively (Figure 4B and Figure 5–figure supplement 1A). In E18.5 liver, FL G1-ILCs mostly distributed at perivascular sites, outside of the sinusoidal lumen (here termed parenchyma) (Figure 4A). In contrast, over 85% of whole ILC1s and NK cells were within sinusoids in AL (Figure 4B and 4C). Although we could not detect IL-7R expression on ILC1s by immunofluorescence, flow cytometry (FCM)-based analysis of intravenous (i.v.) CD45.2 staining confirmed similar intravascular locations of $7R^-$ and $7R^+$ ILC1s as well as NK cells, T cells, and NKT cells in AL (Figure 4D and 4E). In contrast, ILC2s were not efficiently labeled by i.v. staining, consistent with perivascular localization of liver ILC2s observed so far (Dahlgren et al., 2019). Interestingly, a population of AL $Lin^-Sca\text{-}1^+Mac\text{-}1^+$ (LSM) cells, local precursors for ILC1s (Bai et al., 2021), were also not well labeled by i.v. staining. Thus, there are localization shifts between ILC1 precursors and mature ILC1s in the liver: FL G1-ILCs and some LSM cells distribute to parenchyma, whereas AL G1-ILCs including $7R^-$ ILC1s reside within sinusoids. These observations suggest that FL G1-ILCs arise at parenchyma and then infiltrate into sinusoids during maturation toward $7R^-$ ILC1s.

Hepatocyte-derived IL-15 supports the parenchymal development of $7R^-$ ILC1s

Given that the possible origins of FL G1-ILCs and $7R^-$ ILC1s are liver parenchyma, we asked the role of parenchymal microenvironments for ILC1 development. Since IL-15, transpresented as an IL-15/IL-15Rα complex, is a local determinant of G1-ILC homeostasis (Ikuta et al., 2021), we generated IL-15-floxed mice and crossed them with several Cre-driver lines. Reanalysis of single nuclei RNA-seq (snRNA-seq) data of whole liver cells from Liver Cell Atlas (www.livercellatlas.org) revealed that *Il15* gene was highly expressed by macrophages and endothelial cells and, to a lesser extent, by hepatocytes, while *Il15ra* expression was prominent in hepatocytes (Figure 5A, 5B, and Figure 5–figure supplement 1B). We therefore focused on IL-15 produced by hepatocytes, macrophages, and endothelial cells. To target parenchymal IL-15, we generated Alb-Cre IL-15-flox/flox (f/f) mice ($IL\text{-}15^{Alb\text{-}Cre}$ mice), which lacked IL-15 in hepatocytes. In $IL\text{-}15^{Alb\text{-}Cre}$ mice, FL G1-ILCs were significantly reduced (Figure 5C). Notably, $IL\text{-}15^{Alb\text{-}Cre}$ mice also showed reduction of AL

7R$^-$ ILC1s in contrast to unchanged NK cells, 7R$^+$ ILC1s, and NKT cells (Figure 5D, 5E, and Figure 5–figure supplement 1C), despite their similar intravascular localizations. These data corroborate the precursor-progeny relationship of FL G1-ILCs and AL 7R$^-$ ILC1s and also the parenchymal origin of 7R$^-$ ILC1s. To further define the IL-15 niches for G1-ILCs, we generated IL-15$^{Lyve1\text{-}Cre}$ mice, which target vascular IL-15 sources including sinusoidal endothelial cells and a fraction of hematopoietic cells (Lim et al., 2018; Pham et al., 2010). In IL-15$^{Lyve1\text{-}Cre}$ mice, all AL G1-ILC subsets were significantly reduced (Figure 5F). We analyzed another mouse line targeting intravascular IL-15 sources, IL-15$^{LysM\text{-}Cre}$ mice, which lack IL-15 in myeloid cells. IL-15$^{LysM\text{-}Cre}$ mice showed similar two-fold reductions of AL NK cells, 7R$^-$ ILC1s, and 7R$^+$ ILC1s (Figure 5G), confirming the similar IL-15 requirements among all G1-ILC subsets. Notably, expression of Bcl-2, a survival factor downstream of IL-15, was downregulated in all G1-ILCs of IL-15$^{Lyve1\text{-}Cre}$ mice (Figure 5H and 5I), whereas Bcl-2 and Ki-67 levels were unchanged in IL-15$^{Alb\text{-}Cre}$ mice (Figure 5J and 5K). These results indicate that parenchymal IL-15 has no direct impact on mature 7R$^-$ ILC1s in sinusoids whereas intravascular IL-15 directly supports the survival of all AL G1-ILCs. IL-15$^{Alb\text{-}Cre}$ mice had reduced Lin$^-$CD122$^+$CD49a$^+$ ILC1 precursors in AL (Figure 5–figure supplement 1D), suggesting an impaired development of 7R$^-$ ILC1s. Thus, these data demonstrate that hepatocyte-derived IL-15 supports the development of 7R$^-$ ILC1s at parenchyma, thereby maintaining AL 7R$^-$ ILC1s infiltrated in sinusoids.

Steady-state mTOR activity confers granzyme B-mediated cytotoxicity in 7R$^-$ ILC1s

Cytotoxicity is one of the most pivotal functions of G1-ILCs, though the contribution of ILC1s remains controversial. By focusing on the ILC1 heterogeneity, we attempted to describe the G1-ILC effector function in detail. In steady state, minimal levels of granzyme B and death ligands were found on NK cells, while 7R$^-$ ILC1s expressed both granzyme B and TRAIL, the latter of which was also expressed on 7R$^+$ ILC1s (Figure 6A, Figure 6–figure supplement 1A, and 1B) (Friedrich et al., 2021). In line with this, freshly isolated 7R$^-$ ILC1s remarkably lysed multiple tumor cells including YAC-1 (Figure 6B), Hepa1-6 (Figure 6C), and B16F10 cells (Figure 6D). By contrast, NK cells and 7R$^+$ ILC1s showed only slight or no cytotoxicity against these tumor cells, consistent with a previous study showing minimal cytotoxicity of unstimulated NK cells (Fehniger et al., 2007). To determine the effector pathways 7R$^-$ ILC1s rely on, we added concanamycin A (CMA), an inhibitor for perforin/granzyme pathways (Kataoka et al., 1994), and neutralizing antibodies for TRAIL and FasL to the coculture systems. Killing of Hepa1-6 cells by 7R$^-$ ILC1s was markedly

283 inhibited by CMA, and to a lesser extent by anti-TRAIL antibody (Figure 6E). Despite the
284 expression of granzyme A in NK cells and granzyme C in $7R^+$ ILC1s (Nixon et al., 2022)
285 (Figure 6–figure supplement 1C and 1D), CMA had no effect to their cytotoxicity. Other
286 granzyme genes (*Gzmf*, *k*, *n*, and *m*) were undetectable in ILC1s (data not shown). These
287 results suggest that granzyme B plays a major role in the cytotoxicity of $7R^-$ ILC1s.
288 Cellular amount of granzyme B is well correlated to and primarily responsible for the
289 NK cell cytotoxicity (Bhat and Watzl, 2007; Gwalani and Orange, 2018; Prager et al., 2019).
290 Although granzyme B expression and killing capacity of NK cells are weak at steady state,
291 stimulation by cytokines, especially by IL-15, enable to induce both of them (Fehniger et al.,
292 2007; Marçais et al., 2014; Prager et al., 2019). To test whether $7R^-$ ILC1s share such an
293 activation machinery, we analyzed their granzyme B expression after the stimulation. We
294 found that IL-15/IL-15Rα injection more efficiently enhanced granzyme B on NK cells and
295 $7R^+$ ILC1s than $7R^-$ ILC1s, and thereby the granzyme B level on NK cells got comparable to
296 $7R^-$ ILC1s (Figure 6A). IL-15/IL-15Rα also triggered the phosphorylation of STAT5, Akt,
297 and ribosomal protein S6 (a target of mTOR), which are critical for the IL-15-induced effector
298 function (Ali et al., 2015), in NK cells and $7R^+$ ILC1s but to a lesser degree in $7R^-$ ILC1s
299 (Figure 6F, 6G, Figure 6–figure supplement 1E, and 1F). These data suggest that the cytotoxic
300 capacity of $7R^-$ ILC1s are different from that of NK cells in terms of responsiveness and
301 requirement for the cytokine stimulation. Interestingly, the phosphorylation level of S6 was
302 rather higher in ILC1s than NK cells in unstimulated mice (Figure 6F and 6G). Notably,
303 injection of rapamycin, an mTOR complex inhibitor, downregulated granzyme B expression
304 in $7R^-$ ILC1s to a level comparable to that in NK cells (Figure 6H and 6I). By contrast,
305 granzyme B levels in NK cells and $7R^+$ ILC1s were unaffected. Collectively, these results
306 show that $7R^-$ ILC1s exhibit cytotoxicity in their steady state through granzyme B expression,
307 which is supported by their constitutive mTOR activation.
308

Discussion

In this study, we have characterized the developmental process and functional heterogeneity of liver G1-ILCs. Hepatocytes shape IL-15 niches supporting parenchymal development of FL G1-ILCs, that differentiate into 7R$^-$ ILC1s in sinusoids. Functionally, 7R$^-$ ILC1s exhibit granzyme B-mediated cytotoxicity in steady state, in sharp contrast to less cytotoxic resting NK cells.

ILC1 heterogeneity has been extensively addressed recently. In the liver, ILC1s are separated into IL-7R$^-$ and IL-7R$^+$ populations (Friedrich et al., 2021; Sparano et al., 2022; Yomogida et al., 2021), the latter of which can differentiate into the former when cultured *in vitro* or transferred into lymphopenic mice (Friedrich et al., 2021). However, we show that 7R$^-$ and 7R$^+$ ILC1s behave like independent subsets under physiological conditions: decline of 7R$^-$ ILC1s and accumulation of 7R$^+$ ILC1s with age, requirements for RORα specifically in 7R$^+$ ILC1s, and phenotypical stability between 7R$^-$ and 7R$^+$ ILC1s when transferred into WT host mice. Such a contradiction might be due to the highly nutrient- and cytokine-accessible environments in the culture systems and lymphopenic hosts that might trigger non-physiological activation and phenotypic shift of 7R$^+$ ILC1s. Indeed, our model rather gives an explanation for the ILC1 heterogeneity in inflammatory disease models using healthy mice observed so far. In mouse models of contact hypersensitivity, MCMV infection, and liver injury, ILC1s with high expression of cytokine receptors (IL-7R, CD25, and/or IL-18R) highly proliferate and accumulate in AL, thereby forming the memory and protecting liver from infection and injury (Nabekura et al., 2020; Wang et al., 2018; Weizman et al., 2019). AL 7R$^+$ ILC1s resemble such “memory-like” or “activated” ILC1s in terms of the surface phenotype and high proliferation potentials. These observations suggest a hypothesis that a preferential proliferation of pre-existing stable 7R$^+$ ILC1s, rather than inflammation-specific ILC1s induced from naïve ILC1s, may contribute to liver immunity and homeostasis.

Several previous studies have pointed out the precursors for ILC1s: BM iILC1s (Klose et al., 2014), FL G1-ILCs (Constantinides et al., 2015; Daussy et al., 2014), and local precursors in the liver such as LSM cells and Lin$^-$CD122$^+$CD49a$^+$ cells (Bai et al., 2021). In particular, FL G1-ILCs are precursors for AL Ly-49E$^+$ ILC1s (Chen et al., 2022; Sparano et al., 2022). Although AL Ly-49E$^+$ ILC1s are included in and account for 30–40% of AL 7R$^-$ ILC1s, fate-mapping reveals that FL-derived 7R$^-$ ILC1s contain also an Ly49E/F$^-$ population (20–25%), suggesting further heterogeneity in FL-derived ILC1s. Considering the partial contribution (about 50%) of FL G1-ILCs to AL 7R$^-$ ILC1 pool estimated by fate-mapping,

local ILC1 precursors such as LSM cells and $Lin^{-}CD122^{+}CD49a^{+}$ cells might be the other sources for $7R^{-}$ ILC1s. By contrast, the origin of AL $7R^{+}$ ILC1s remains to be solved. We show that BM iILC1s have a potential to differentiate into AL $7R^{+}$ ILC1s, but the actual contribution is unclear. As both AL $7R^{-}$ and $7R^{+}$ ILC1s were rarely replaced during parabiosis experiments using adult mice, it is possible that a transiently migrated population derived from BM settle and give rise to $7R^{+}$ ILC1s in the liver during neonatal period, as discussed previously (Sparano et al., 2022). Further investigations using a specific tracing approach such as fate-mapping of BM iILC1s are required to determine their precise developmental potency.

Development and maintenance of ILCs strictly depend on their resident tissue microenvironments, called niche (Ikuta et al., 2021; Kotas and Locksley, 2018; McFarland and Colonna, 2020; Murphy et al., 2022). IL-15 is a cytokine crucial for G1-ILC homeostasis. IL-15-producing cells shape the niches for G1-ILCs within various tissues via the IL-15/IL-15Rα transpresentation (Cepero-Donates et al., 2016; Cui et al., 2014; Liou et al., 2014; Mortier et al., 2009), yet IL-15 niches specific for ILC1s remained unclear. Using a combination of imaging and cell-specific IL-15 knockout approaches, we unveil the parenchymal origins of $7R^{-}$ ILC1s as well as FL G1-ILCs and identify hepatocytes as an IL-15-producing niche supporting $7R^{-}$ ILC1 development. Parenchymal distribution of FL G1-ILCs, reminiscent of FL hematopoietic stem cells (HSCs) (Khan et al., 2016; Lewis et al., 2021), might be partly due to the immaturity of hepatic vasculature in that period. Since FL G1-ILCs and FL HSCs are also similar in that they eventually infiltrate into blood vessels (Lewis et al., 2021), it would be of interest to address the mechanism underlying their neonatal dynamics. In addition, it is still unclear why hepatocyte-derived IL-15 has such a local effect despite many fenestrae and the lack of a basement membrane on liver sinusoids. One possible explanation is that the transpresentation of IL-15/IL-15Rα by hepatocytes may require direct contact to target cells, as dendritic cells do (Mortier et al., 2008). Given that hepatocytes prominently express *Il15ra* gene and its deletion results in the reduction of whole IL-15-dependent lymphocytes in the liver (Cepero-Donates et al., 2016), it is also possible that hepatocytes may produce IL-15Rα as a soluble form, that binds to other cell-derived IL-15 to exert non-local effects.

Traditionally, ILC1s are regarded as less cytotoxic than NK cells in mice, whereas recent studies have challenged this theory (Dadi et al., 2016; Di Censo et al., 2021; Kansler et al., 2022; Nixon et al., 2022; Yomogida et al., 2021). Our study provides two possible

explanations for this discrepancy. First, the age of mice selected for analysis influence the composition and overall cytotoxicity of ILC1s. We and others (Chen et al., 2022; Friedrich et al., 2021; Nixon et al., 2022) showed that ILC1s were heterogenous in their cytotoxicity. Due to the age-dependent reduction of highly cytotoxic $7R^-$ ILC1s, the overall cytotoxicity of ILC1s in the liver should decline with age. Second, the effector program of $7R^-$ ILC1s differ from NK cells in its nature, especially in terms of cytokine responsiveness. Freshly isolated NK cells exhibit low expression of cytotoxic molecules and only minimal cytotoxicity (Fehniger et al., 2007), while stimulation by IL-15 confers granzyme B expression and cytotoxicity on NK cells via mTOR-dependent metabolic reprogramming (Marçais et al., 2014; Nandagopal et al., 2014). Conversely, we show that $7R^-$ ILC1s exhibit prominent granzyme B-mediated cytotoxicity via mTOR activity at steady state, though they are less responsive to cytokines than NK cells and $7R^+$ ILC1s. These findings suggest that $7R^-$ ILC1s are "ready-to-kill" sentinels that contribute to the tonic immune surveillance, which is followed later by the response of activated and proliferated NK cells and $7R^+$ ILC1s.

Taken together, our study provides insight into the complex ILC1 ontogeny by revealing relationships among heterogenous ILC1 subsets, their developmental dynamics, and niche dependence. Our findings highlight the intrinsic cytotoxic programs of $7R^-$ ILC1s unlike NK cells, proposing them as critical steady-state sentinels against infection prevention and tumor surveillance and bringing the possibility of local therapeutic targeting of ILC1 function.

Materials and Methods

Mice

C57BL/6J mice were purchased from Japan SLC (Hamamatsu, Japan). IL-7$^{-/-}$ mice were obtained by IL-7-flox mice developed in our laboratory (Liang et al., 2012) with Cre-mediated germ-line deletion. PLZF-IRES-EGFP-Cre (Constantinides et al., 2014) mice were provided by Dr. M. Miyazaki at Kyoto University and crossed with Rosa26-YFP mice (Srinivas et al., 2001). RORα knockout (RORα$^{-/-}$) mice were generated by CRISPR/Cas9 gene editing in our laboratory and will be reported in detail elsewhere. CXCR6-GFP KI (CXCR6$^{GFP/+}$) mice were provided by Dr. H. Ohno. IL-15-flox mice were generated in our laboratory (Cui et al., under review) and bred with Alb-Cre mice (Postic et al., 1999) and Lyve1-Cre mice (Pham et al., 2010), which were kindly supplied by Dr. Mark A. Magnuson at Vanderbilt University and by Dr. Jason Cyster at University of California San Francisco, respectively. NKp46-CreERT2 Tg mice (Nabekura and Lanier, 2016) were provided by Dr. T. Nabekura and Dr. Lewis L. Lanier and crossed with Rosa26-tdTomato (Madisen et al., 2010) mice. For fetal experiments, the noon when the vaginal plug was detected was considered as embryonic day (E) 0.5. All mice were maintained under specific pathogen-free conditions in the Experimental Research Center for Infectious Diseases at the Institute for Life and Medical Sciences, Kyoto University. All procedures were carried out under sevoflurane or isoflurane anesthesia to minimize animal suffering. All mouse protocols were approved by the Animal Experimentation Committee of the Institute for Life and Medical Sciences, Kyoto University.

Cell preparation and isolation

To protect ILC1s from NAD$^+$-induced cell death (NICD) (Stark et al., 2018), mice were intravenously (i.v.) injected with 40 μg ARTC2.2 blocking nanobody (BioLegend, San Diego, CA, USA) 30 min before sacrificing the mice in several experiments. Fetal liver, adult liver, spleen, peripheral (axillary, brachial, and inguinal) lymph nodes, and mesenteric lymph nodes were dissociated mechanically and passed through 70-μm cell strainers (Greiner Bio-One, Milan, Italy). Adult liver leukocytes were then separated by centrifugation through 40% Percoll. Peritoneal cavity was washed by 5 mL of PBS and the wash fluid was extracted using a syringe and a 21 G needle (Terumo Corporation, Tokyo, Japan). BM cells were obtained by flushing out the marrow fraction of femurs and tibias. To collect salivary gland cells, submandibular and sublingual glands were minced with scissors and incubated at 37℃ for 1

hour in RPMI 1640 medium containing 10% fetal bovine serum, 1 mg/mL collagenase D, and 50 μg/mL DNase I (Sigma-Aldrich, St. Luis, MO, USA). The cell suspension was filtered through a 70-μm cell strainer and purified using 40% Percoll. For the isolation of intestinal lamina propria lymphocytes, small intestines were flushed out and Peyer's patches were excised. The intestines were opened longitudinally, cut into 1-cm pieces, and incubated at 37°C for 30 min in PBS with 5 mM EDTA to remove epithelial cells. The incubated pieces were then minced and digested by RPMI 1640 medium containing 10% fetal bovine serum, 1.25 mg/mL collagenase D, and 50 μg/mL DNase I. The tissue suspension was passed through a 70-μm cell strainer and lymphocytes were purified by 40% Percoll.

Flow cytometry and cell sorting

Following fluorescent dye- or biotin-conjugated antibodies (BioLegend, San Diego, CA, USA; Thermo Fisher Scientific, Waltham, MA, USA; BD Bioscience, San Jose, CA, USA; TONBO Biosciences, San Diego, CA, USA) were used: CD3ε (145-2C11), NK1.1 (PK136), NKp46 (29A1.4), CD49a (HMα1), CD49b (DX5), IL-7Rα (A7R34), CXCR6 (SA051D1), TRAIL (N2B2), CD69 (H1.2F3), CD200R (OX-110), CXCR3 (CXCR3-173), CD25 (PC61), Thy-1.2 (30-H12), KLRG1 (2F1/KLRG1), CD11b (M1/70), CD62L (MEL-14), Eomes (Dan11mag), T-bet (4B10), CD45.1 (A20), CD45.2 (104), CD45 (30-F11), Ki-67 (SolA15), Bcl-2 (BCL/10C4), CD31 (MEC13.3), LYVE-1 (LVY7), CD122 (TM-β1), Ter119 (Ter119), F4/80 (BM8), Gr-1 (RB6-8C5), CD19 (6D5), B220 (RA3-6B2), TCRβ (H57–597), FcεRI (MAR-1), PD-1 (29F.1A12), α4β7 (DATK32), Sca-1 (E13-161.7), c-Kit (2B8), Flt3 (A2F10), granzyme B (NGZB), granzyme C (SFC1D8), FasL (MFL3), Ly49E/F (CM4), p-S6 (D57.2.2E), p-STAT5 (47), and p-Akt (S473) (M89-61). Biotinylated monoclonal antibodies were detected with APC- or Brilliant Violet 421-conjugated streptavidin (Thermo Fisher Scientific). For intracellular staining of Eomes, T-bet, Bcl-2, Ki-67, and granzymes, cells were stained for surface antigens, fixed, permeabilized, and stained using Foxp3 Staining Buffer Set or IC Fixation Buffer (Thermo Fisher Scientific). For intracellular staining of p-S6, p-STAT5, and p-Akt (S473), cells were stained for surface antigens, fixed, permeabilized, and stained using BD Phosflow Buffer (BD Biosciences). Flow cytometry and cell sorting were performed on BD FACSVerse or BD LSRFortessa X-20 flow cytometers (BD Biosciences) and BD FACS Aria II or Aria III cell sorters (BD Biosciences), respectively. Data were analyzed on FlowJo software (FlowJo, Ashland, OR, USA). Debris and dead cells were excluded from analysis by forward and side scatter and propidium iodide (PI) gating. In

figures, values in quadrants, gated areas, and interval gates indicate percentages in each population.

Fate-mapping experiment

Fate-mapping of ILCPs in BM or FL were performed as described previously (Constantinides et al., 2014). In brief, 1×10^4 $YFP^-Lin^-Sca1^+c\text{-}Kit^+$ (LSK) cells isolated from BM or FL of PLZF-GFP-Cre Rosa26-YFP mice were injected i.v. into lethally (9 Gy) irradiated CD45.1 WT mice to remove the random YFP labelling occurred prior to the hematopoiesis. The recipient mice were analyzed 5 weeks after the transplantation. Straight PLZF-GFP-Cre Rosa26-YFP mice were also analyzed to confirm the results. For fate-mapping of FL G1-ILCs in NKp46-CreERT2 Rosa26-tdTomato mice, 4 mg tamoxifen (Sigma-Aldrich) was intraperitoneally injected into pregnant mothers at E17.5. Neonatal (postnatal day 0–4) and 4 weeks old pups were analyzed.

RNA sequencing (RNA-seq) and data analysis

For bulk RNA-seq, freshly sorted G1-ILC populations (1×10^3 cells) were lysed with Buffer RLT (Qiagen, Hilden, Germany) and purified with RNAClean XP (Beckman Coulter, Brea, CA, USA). Double strand cDNA was synthesized, and sequencing libraries were constructed using SMART-seq HT Plus kit (Takara Bio, Otsu, Japan). Sequencing was performed with 150 bp paired-end reads on the Illumina HiSeq X sequencer (Illumina, San Diego, CA, USA). fastp (Chen et al., 2018) was used to assess sequencing quality and to exclude low-quality reads and adaptor contaminations. Reads were mapped on the mouse reference genome (mm10) using HiSat2. The read counts were determined at the gene level with featureCounts. Normalization of gene expression levels and differential gene expression analysis were performed using DESeq2. Genes were considered as differentially expressed genes (DEG) when they had an adjusted p (p_{adj}) value < 0.05 and fold changes > 1.0. Metascape (Zhou et al., 2019) and gene set enrichment analysis (GSEA, Broad Institute) was used for enrichment analysis. For reanalysis of single nuclei RNA-seq (snRNA-seq) data of whole liver cells in mice (Liver Cell Atlas; www.livercellatlas.org), normalization, scaling, and UMAP clustering using first 5 dimensions in principal component analysis (PCA) of scaled count matrix were performed on R package Seurat 4.0.2.

***In vivo* treatment**

For *in vivo* stimulation of G1-ILCs, mice were administrated intraperitoneally (i.p.) with 2 μg IL-15/IL-15Rα complex (the RLI form as in Mortier et al., 2006, provided by Dr. J. M. Dijkstra) once a day. After 18 hours, liver cells were isolated and analyzed by flow cytometry to detect cytotoxic molecule expression. For rapamycin treatment, 30 μg rapamycin in 100 μL corn oil was injected i.p. into mice 18 hours before the analysis.

Intrasplenic injection

A small incision was made on the left flank of anesthetized mice and the lower pole of the spleen was gently exposed. Cell suspension (50 μL) was slowly injected into the spleen by a 0.3 mL insulin syringe with a 29 G needle (BD Biosciences). Cotton wool was applied to the spleen for several minutes after the injection to stop bleeding.

Adoptive transfer experiments

NK cells, $7R^-$ ILC1s, $7R^+$ ILC1s, and BM iILC1s (2×10^4–5×10^4 cells) and FL G1-ILCs (1×10^5 cells) were sorted from adult and E18.5 CD45. 1 WT mice, respectively. Each G1-ILC population was adoptively transferred into CD45.2 WT mice by intrasplenic injection. At the indicated time points, cells were isolated from the liver of recipient mice and analyzed by flow cytometry. To assess the stability and the proliferation capacity of $7R^-$ ILC1s and $7R^+$ ILC1s in inflammatory conditions, CD45.2 WT mice were injected with indicated G1-ILC populations labeled by Cell Proliferation Dye (CPD) eFluor 450 (Thermo Fisher Scientific) (day 0) followed by the administration of 2 μg IL-15/IL-15Rα at day 1, 3, and 5. After 7 days, liver leukocytes of recipient mice were analyzed.

Immunofluorescence

Whole FL of WT mice or hepatic lobes of adult CXCR6-GFP KI mice were fixed with 4% paraformaldehyde (PFA) at 4°C for 6 hours, embedded in Optimal Cutting Temperature compound (Sakura Finetechnical, Tokyo, Japan), and sliced with a cryomicrotome (Leica CM3050S, Wetzlar, Germany). Tissue sections were stained at room temperature for 1 hour with primary antibodies as follows: biotin-anti-CD31, rabbit polyclonal IgG anti-LYVE-1 (RELIATech, Braunschweig, Germany), and goat polyclonal IgG anti-NKp46 (R&D, Minneapolis, MN, USA). Following secondary antibodies (BioLegend) were used: Dylight 488 anti-rabbit IgG, Alexa Fluor 555 anti-rabbit IgG, Alexa Fluor 647 anti-goat IgG, Brilliant Violet 421 anti-rabbit IgG, Dylight 649 anti-rat IgG, and PE anti-rat IgG. Biotinylated

antibodies were detected with FITC-, PE-, or Brilliant Violet 421-conjugated streptavidin (Thermo Fisher Scientific). Stained sections were then mounted using PermaFluor Aqueous Mounting Medium (Thermo Fisher Scientific) and examined by a TCS SP8 confocal microscope (Leica) with HC PLAPO CS2 20×/0.75 IMM or HC PLAPO CS2 40×/1.30 OIL object lenses. Multiple image stacks (10–20 μm) were acquired with two times of frame averaging and maximum projection was then performed on using LAS X software (Leica).

Intravascular staining

PE/Cy7 anti-CD45.2 antibody (clone: 104) (2 μg) was injected intravenously (i.v.) into mice 2 min before the perfusion and liver dissection. Isolated liver leukocytes were stained with fluorophore-conjugated antibodies of interest in addition to APC/Cy7 anti-CD45 antibody (clone: 30-F11) and analyzed by flow cytometry.

Parabiosis

Female CD45.1 and CD45.2 congenic C57BL/6J mice were surgically conjoined as previously described (Gasteiger et al., 2015). In brief, lateral skin from elbow to knee of each mouse was sutured, forelimbs and hindlimbs were tied together, and the skin incisions were closed using surgical adhesive. After 60 days of surgery, mice were analyzed by flow cytometry.

***In vitro* killing assay**

Hepa1-6 cells were purchased from RIKEN BioResource Center (RIKEN BRC, Tsukuba, Japan). B16F10 cells were provided by Dr. T. Honjo at Kyoto University. These mouse tumor cell lines were maintained in Dulbecco's modified Eagle's medium (DMEM) supplemented with 10% FBS, 2 mM L-glutamine, and antibiotics. For time-lapse killing assays, 2×10^2 Hepa1-6 cells or B16F10 cells were labeled by CPD eFluor 450 and pre-incubated with RPMI 1640 medium (without phenol red) containing 10% FBS, 10 mM HEPES (pH7.4), antibiotics, and 1 μg/mL PI on 96-well round bottom plates. Freshly sorted liver NK cells, $7R^-$ ILC1s, or $7R^+$ ILC1s (2×10^3 cells) were added to the plates and co-cultured with tumor cells. Time-lapse imaging was performed using a BZ-X710 microscope (Keyence, Osaka, Japan) with CFI Plan Apo λ 10× and CFI Plan Fluor DL 10× objective lenses at a 20 min interval for up to 6 hours. To determine the contribution of effector molecules, 50 nM concanamycin A (CMA), 10 μg/mL anti-TRAIL antibody (N2B2), or 10 μg/mL anti-FasL antibody (MFL3)

were supplemented and compared to vehicle-supplemented controls. Tumor cell viability was defined by the ratio of the CPD^+PI^- viable tumor cell number at each time point to the viable tumor cell number at the beginning of the imaging and represented as the moving average of three consecutive time points. Image analysis and cell counts were performed using BZ-X Analyzer (Keyence). For killing assay of YAC-1 cells (provided by Dr. M. Hattori at Kyoto University), 2×10^4 freshly sorted liver NK cells, $7R^-$ ILC1s, or $7R^+$ ILC1s were co-cultured for 4 hours with 2×10^3 CPD eFluor 450-labeled YAC-1 cells in RPMI 1640 medium containing 10% FBS, 10 mM HEPES (pH7.4), and antibiotics. After culture, YAC-1 cells were stained with FITC-conjugated Annexin V and PI (MEBCYTO-Apoptosis Kit, MBL) and the ratio of Annexin V^+PI^+ apoptotic cells were analyzed by flow cytometry.

Statistical analysis

Statistical differences were evaluated by the two-tailed unpaired Student's *t*-test and one-way or two-way analysis of variance (ANOVA) using GraphPad Prism 8 (GraphPad Software, San Diego, California, USA). Asterisks in all figures indicate as follows: $*p < 0.05$, $**p < 0.01$, $***p < 0.001$, and $****p < 0.0001$.

Acknowledgments

We acknowledge Dr. Lewis L. Lanier for providing NKp46-CreERT2 mice, Dr. Mark A. Magnuson for Alb-Cre mice, Dr. Jason Cyster for Lyve1-Cre mice, and members of the K. Ikuta laboratory for discussion and supervision. Time-lapse imaging using Keyence BZ-X710 microscope were performed at the Medical Research Support Center, Graduate School of Medicine, Kyoto University, which was supported by Platform for Drug Discovery, Informatics, and Structural Life Science from the Ministry of Education, Culture, Sports, Science and Technology, Japan.

Funding: This research was supported by the Japan Society for the Promotion of Science (JSPS) KAKENHI grant numbers 20H03501 and 20K21525 (K.I.), 19K16687 and 21K07067 (G.C.). It is also supported by a grant from Takeda Science Foundation to A.S., by grants from the Shimizu Foundation for Immunology and Neuroscience to T.A. and A.S., and by the Joint Usage/Research Center program of Institute for Life and Medical Sciences Kyoto University.

Author contributions: T.A., S.A., G.C., and K.I. designed the research. T.A., S.A., G.C., A.S., and K.O. performed the animal experiments, flow cytometry, and analyzed the data. T.N., A.S., and M.M. designed and supervised fate-mapping studies. H.M. and S.K. performed the surgery of parabiosis and cesarean section of mice. J.D. contributed to *in vivo* stimulation experiments using IL-15/IL-15Rα. H.O. supported immunofluorescence experiments. T.A. and K.I. wrote the manuscript. All authors read and approved the final version of the manuscript.

Competing interests

All authors declare no competing interests.

Data availability

All data needed to evaluate the conclusions in the paper are present in the paper. RNA-seq data generated in this study are deposited in Gene Expression Omnibus (GEO) under accession code GSE205894.

612 **References**

613

614 Ali, A.K., N. Nandagopal, and S.H. Lee. 2015. IL-15-PI3K-AKT-mTOR: a critical pathway in
615 the life journey of natural killer cells. *Front. Immunol.* 6:355.

616 Bai, L., M. Vienne, L. Tang, Y. Kerdiles, M. Etiennot, B. Escalière, J. Galluso, H. Wei, R. Sun,
617 E. Vivier, H. Peng, and Z. Tian. 2021. Liver type 1 innate lymphoid cells develop
618 locally via an interferon-γ-dependent loop. *Science* 371:eaba4177.

619 Bhat, R., and C. Watzl. 2007. Serial killing of tumor cells by human natural killer cells--
620 enhancement by therapeutic antibodies. *PLoS One* 2:e326.

621 Cepero-Donates, Y., V. Rakotoarivelo, M. Mayhue, A. Ma, Y.-G. Chen, and S. Ramanathan.
622 2016. Homeostasis of IL-15 dependent lymphocyte subsets in the liver. *Cytokine*
623 82:95-101.

624 Chen, S., Y. Zhou, Y. Chen, and J. Gu. 2018. fastp: an ultra-fast all-in-one FASTQ
625 preprocessor. *Bioinformatics* 34:i884-i890.

626 Chen, Y., X. Wang, X. Hao, B. Li, W. Tao, S. Zhu, K. Qu, H. Wei, R. Sun, H. Peng, and Z.
627 Tian. 2022. Ly49E separates liver ILC1s into embryo-derived and postnatal subsets
628 with different functions. *J. Exp. Med.* 219:e20211805.

629 Constantinides, M.G., H. Gudjonson, B.D. McDonald, I.E. Ishizuka, P.A. Verhoef, A.R.
630 Dinner, and A. Bendelac. 2015. PLZF expression maps the early stages of ILC1
631 lineage development. *Proc. Natl. Acad. Sci. USA.* 112:5123-5128.

632 Constantinides, M.G., B.D. McDonald, P.A. Verhoef, and A. Bendelac. 2014. A committed
633 precursor to innate lymphoid cells. *Nature* 508:397-401.

634 Cui, G., T. Hara, S. Simmons, K. Wagatsuma, A. Abe, H. Miyachi, S. Kitano, M. Ishii, S.
635 Tani-Ichi, and K. Ikuta. 2014. Characterization of the IL-15 niche in primary and
636 secondary lymphoid organs in vivo. *Proc. Natl. Acad. Sci. USA.* 111:1915-1920.

637 Dadi, S., S. Chhangawala, B.M. Whitlock, R.A. Franklin, C.T. Luo, S.A. Oh, A. Toure, Y.
638 Pritykin, M. Huse, C.S. Leslie, and M.O. Li. 2016. Cancer immunosurveillance by
639 tissue-resident innate lymphoid cells and innate-like T cells. *Cell* 164:365-377.

Dahlgren, M.W., S.W. Jones, K.M. Cautivo, A. Dubinin, J.F. Ortiz-Carpena, S. Farhat, K.S. Yu, K. Lee, C. Wang, A.V. Molofsky, A.D. Tward, M.F. Krummel, T. Peng, and A.B. Molofsky. 2019. Adventitial stromal cells define group 2 innate lymphoid cell tissue niches. *Immunity* 50:707-722.e706.

Daussy, C., F. Faure, K. Mayol, S. Viel, G. Gasteiger, E. Charrier, J. Bienvenu, T. Henry, E. Debien, U.A. Hasan, J. Marvel, K. Yoh, S. Takahashi, I. Prinz, S. de Bernard, L. Buffat, and T. Walzer. 2014. T-bet and Eomes instruct the development of two distinct natural killer cell lineages in the liver and in the bone marrow. *J. Exp. Med.* 211:563-577.

Di Censo, C., M. Marotel, I. Mattiola, L. Müller, G. Scarno, G. Pietropaolo, G. Peruzzi, M. Laffranchi, J. Mazej, M.S. Hasim, S. Asif, E. Russo, L. Tomaipitinca, H. Stabile, S.H. Lee, L. Vian, M. Gadina, A. Gismondi, H.Y. Shih, Y. Mikami, C. Capuano, G. Bernardini, M. Bonelli, S. Sozzani, A. Diefenbach, M. Ardolino, A. Santoni, and G. Sciumè. 2021. Granzyme A and CD160 expression delineates ILC1 with graded functions in the mouse liver. *Eur. J. Immunol.* 51:2568-2575.

Fehniger, T.A., S.F. Cai, X. Cao, A.J. Bredemeyer, R.M. Presti, R. French, Anthony, and T.J. Ley. 2007. Acquisition of murine NK cell cytotoxicity requires the translation of a pre-existing pool of granzyme B and perforin mRNAs. *Immunity* 26:798-811.

Friedrich, C., R.L.R.E. Taggenbrock, R. Doucet-Ladevèze, G. Golda, R. Moenius, P. Arampatzi, N.A.M. Kragten, K. Kreymborg, M. Gomez De Agüero, W. Kastenmüller, A.-E. Saliba, D. Grün, K.P.J.M. Van Gisbergen, and G. Gasteiger. 2021. Effector differentiation downstream of lineage commitment in ILC1s is driven by Hobit across tissues. *Nat. Immunol.* 22:1256-1267.

Gasteiger, G., X. Fan, S. Dikiy, S.Y. Lee, and A.Y. Rudensky. 2015. Tissue residency of innate lymphoid cells in lymphoid and nonlymphoid organs. *Science* 350:981-985.

Gwalani, L.A., and J.S. Orange. 2018. Single degranulations in NK Cells can mediate target cell killing. *J. Immunol.* 200:3231-3243.

Ikuta, K., T. Hara, S. Abe, T. Asahi, D. Takami, and G. Cui. 2021. The roles of IL-7 and IL-15 in niches for lymphocyte progenitors and immune cells in lymphoid organs. *Curr. Top. Microbiol. Immunol.* 434:83-101.

670 Jacquelot, N., C. Seillet, E. Vivier, and G.T. Belz. 2022. Innate lymphoid cells and cancer. *Nat.*
671 *Immunol.* 23:371-379.

672 Kansler, E.R., S. Dadi, C. Krishna, B.G. Nixon, E.G. Stamatiades, M. Liu, F. Kuo, J. Zhang,
673 X. Zhang, K. Capistrano, K.A. Blum, K. Weiss, R.M. Kedl, G. Cui, K. Ikuta, T.A.
674 Chan, C.S. Leslie, A.A. Hakimi, and M.O. Li. 2022. Cytotoxic innate lymphoid cells
675 sense cancer cell-expressed interleukin-15 to suppress human and murine
676 malignancies. *Nat. Immunol.* 23:904-915.

677 Kataoka, T., K. Takaku, J. Magae, N. Shinohara, H. Takayama, S. Kondo, and K. Nagai. 1994.
678 Acidification is essential for maintaining the structure and function of lytic granules of
679 CTL. Effect of concanamycin A, an inhibitor of vacuolar type H(+)-ATPase, on CTL-
680 mediated cytotoxicity. *J. Immunol.* 153:3938-3947.

681 Khan, J.A., A. Mendelson, Y. Kunisaki, A. Birbrair, Y. Kou, A. Arnal-Estapé, S. Pinho, P.
682 Ciero, F. Nakahara, A. Ma'ayan, A. Bergman, M. Merad, and P.S. Frenette. 2016. Fetal
683 liver hematopoietic stem cell niches associate with portal vessels. *Science* 351:176-
684 180.

685 Klose, C.S.N., M. Flach, L. Möhle, L. Rogell, T. Hoyler, K. Ebert, C. Fabiunke, D. Pfeifer, V.
686 Sexl, D. Fonseca-Pereira, R.G. Domingues, H. Veiga-Fernandes, S.J. Arnold, M.
687 Busslinger, I.R. Dunay, Y. Tanriver, and A. Diefenbach. 2014. Differentiation of type 1
688 ILCs from a common progenitor to all helper-like innate lymphoid cell lineages. *Cell*
689 157:340-356.

690 Kotas, M.E., and R.M. Locksley. 2018. Why innate lymphoid cells? *Immunity* 48:1081-1090.

691 Krabbendam, L., J.H. Bernink, and H. Spits. 2021. Innate lymphoid cells: from helper to killer.
692 *Curr Opin Immunol* 68:28-33.

693 Lewis, K., M. Yoshimoto, and T. Takebe. 2021. Fetal liver hematopoiesis: from development
694 to delivery. *Stem Cell Res. Ther.* 12:139.

695 Liang, B., T. Hara, K. Wagatsuma, J. Zhang, K. Maki, H. Miyachi, S. Kitano, C. Yabe-
696 Nishimura, S. Tani-Ichi, and K. Ikuta. 2012. Role of hepatocyte-derived IL-7 in
697 maintenance of intrahepatic NKT cells and T cells and development of B cells in fetal
698 liver. *J. Immunol.* 189:4444-4450.

699 Lim, H.Y., S.Y. Lim, C.K. Tan, C.H. Thiam, C.C. Goh, D. Carbajo, S.H.S. Chew, P. See, S.
700 Chakarov, X.N. Wang, L.H. Lim, L.A. Johnson, J. Lum, C.Y. Fong, A. Bongso, A.
701 Biswas, C. Goh, M. Evrard, K.P. Yeo, R. Basu, J.K. Wang, Y. Tan, R. Jain, S. Tikoo, C.
702 Choong, W. Weninger, M. Poidinger, R.E. Stanley, M. Collin, N.S. Tan, L.G. Ng, D.G.
703 Jackson, F. Ginhoux, and V. Angeli. 2018. Hyaluronan receptor LYVE-1-expressing
704 macrophages maintain arterial tone through hyaluronan-mediated regulation of smooth
705 muscle cell collagen. *Immunity* 49:326-341.e327.

706 Liou, Y.-H., S.-W. Wang, C.-L. Chang, P.-L. Huang, M.-S. Hou, Y.-G. Lai, G.A. Lee, S.-T.
707 Jiang, C.-Y. Tsai, and N.-S. Liao. 2014. Adipocyte IL-15 regulates local and systemic
708 NK cell development. *J. Immunol.* 193:1747-1758.

709 Lodolce, J.P., D.L. Boone, S. Chai, R.E. Swain, T. Dassopoulos, S. Trettin, and A. Ma. 1998.
710 IL-15 receptor maintains lymphoid homeostasis by supporting lymphocyte homing
711 and proliferation. *Immunity* 9:669-676.

712 Madisen, L., T.A. Zwingman, S.M. Sunkin, S.W. Oh, H.A. Zariwala, H. Gu, L.L. Ng, R.D.
713 Palmiter, M.J. Hawrylycz, A.R. Jones, E.S. Lein, and H. Zeng. 2010. A robust and
714 high-throughput Cre reporting and characterization system for the whole mouse brain.
715 *Nat. Neurosci.* 13:133-140.

716 Marçais, A., J. Cherfils-Vicini, C. Viant, S. Degouve, S. Viel, A. Fenis, J. Rabilloud, K. Mayol,
717 A. Tavares, J. Bienvenu, Y.G. Gangloff, E. Gilson, E. Vivier, and T. Walzer. 2014. The
718 metabolic checkpoint kinase mTOR is essential for IL-15 signaling during the
719 development and activation of NK cells. *Nat. Immunol.* 15:749-757.

720 McFarland, A.P., and M. Colonna. 2020. Sense and immuno-sensibility: innate lymphoid cell
721 niches and circuits. *Curr. Opin. Immunol.* 62:9-14.

722 McFarland, A.P., A. Yalin, S.Y. Wang, V.S. Cortez, T. Landsberger, R. Sudan, V. Peng, H.L.
723 Miller, B. Ricci, E. David, R. Faccio, I. Amit, and M. Colonna. 2021. Multi-tissue
724 single-cell analysis deconstructs the complex programs of mouse natural killer and
725 type 1 innate lymphoid cells in tissues and circulation. *Immunity* 54:1320-1337.e1324.

726 Mortier, E., R. Advincula, L. Kim, S. Chmura, J. Barrera, B. Reizis, B.A. Malynn, and A. Ma.
727 2009. Macrophage- and dendritic-cell-derived interleukin-15 receptor alpha supports
728 homeostasis of distinct $CD8^+$ T cell subsets. *Immunity* 31:811-822.

729 Mortier, E., T. Woo, R. Advincula, S. Gozalo, and A. Ma. 2008. IL-15Ralpha chaperones IL-
730 15 to stable dendritic cell membrane complexes that activate NK cells via trans
731 presentation. *J. Exp. Med.* 205:1213-1225.

732 Murphy, J.M., L. Ngai, A. Mortha, and S.Q. Crome. 2022. Tissue-dependent adaptations and
733 functions of innate lymphoid cells. *Front. Immunol.* 13:836999.

734 Nabekura, T., and L.L. Lanier. 2016. Tracking the fate of antigen-specific versus cytokine-
735 activated natural killer cells after cytomegalovirus infection. *J. Exp. Med.* 213:2745-
736 2758.

737 Nabekura, T., L. Riggan, A.D. Hildreth, T.E. O'Sullivan, and A. Shibuya. 2020. Type 1 innate
738 lymphoid cells protect mice from acute liver injury via interferon-γ secretion for
739 upregulating Bcl-xL expression in hepatocytes. *Immunity* 52:96-108.e109.

740 Nandagopal, N., A.K. Ali, A.K. Komal, and S.H. Lee. 2014. The critical role of IL-15-PI3K-
741 mTOR pathway in natural killer cell effector functions. *Front. Immunol.* 5:187.

742 Nixon, B.G., C. Chou, C. Krishna, S. Dadi, A.O. Michel, A.E. Cornish, E.R. Kansler, M.H.
743 Do, X. Wang, K.J. Capistrano, A.Y. Rudensky, C.S. Leslie, and M.O. Li. 2022.
744 Cytotoxic granzyme C-expressing ILC1s contribute to antitumor immunity and
745 neonatal autoimmunity. *Sci. Immunol.* 7:eabi8642.

746 Peng, H., X. Jiang, Y. Chen, D.K. Sojka, H. Wei, X. Gao, R. Sun, W.M. Yokoyama, and Z.
747 Tian. 2013. Liver-resident NK cells confer adaptive immunity in skin-contact
748 inflammation. *J. Clin. Invest.* 123:1444-1456.

749 Pham, T.H.M., P. Baluk, Y. Xu, I. Grigorova, A.J. Bankovich, R. Pappu, S.R. Coughlin, D.M.
750 Mcdonald, S.R. Schwab, and J.G. Cyster. 2010. Lymphatic endothelial cell
751 sphingosine kinase activity is required for lymphocyte egress and lymphatic patterning.
752 *J. Exp. Med.* 207:17-27.

753 Postic, C., M. Shiota, K.D. Niswender, T.L. Jetton, Y. Chen, J.M. Moates, K.D. Shelton, J.
754 Lindner, A.D. Cherrington, and M.A. Magnuson. 1999. Dual roles for glucokinase in
755 glucose homeostasis as determined by liver and pancreatic β cell-specific gene knock-
756 outs using Cre recombinase. *J. Biol. Chem.* 274:305-315.

Prager, I., C. Liesche, H. van Ooijen, D. Urlaub, Q. Verron, N. Sandström, F. Fasbender, M. Claus, R. Eils, J. Beaudouin, B. Önfelt, and C. Watzl. 2019. NK cells switch from granzyme B to death receptor-mediated cytotoxicity during serial killing. *J Exp Med* 216:2113-2127.

Robinette, M.L., J.K. Bando, W. Song, T.K. Ulland, S. Gilfillan, and M. Colonna. 2017. IL-15 sustains IL-7R-independent ILC2 and ILC3 development. *Nat. Commun.* 8:14601.

Sojka, D.K., B. Plougastel-Douglas, L. Yang, M.A. Pak-Wittel, M.N. Artyomov, Y. Ivanova, C. Zhong, J.M. Chase, P.B. Rothman, J. Yu, J.K. Riley, J. Zhu, Z. Tian, and W.M. Yokoyama. 2014. Tissue-resident natural killer (NK) cells are cell lineages distinct from thymic and conventional splenic NK cells. *Elife* 3:e01659.

Song, J., H. Song, H. Wei, R. Sun, Z. Tian, and H. Peng. 2021. Requirement of RORα for maintenance and antitumor immunity of liver-resident natural killer cells/ILC1s. *Hepatology* 75:1181-1193.

Sparano, C., D. Solís-Sayago, A. Vijaykumar, C. Rickenbach, M. Vermeer, F. Ingelfinger, G. Litscher, A. Fonseca, C. Mussak, M. Mayoux, C. Friedrich, C. Nombela-Arrieta, G. Gasteiger, B. Becher, and S. Tugues. 2022. Embryonic and neonatal waves generate distinct populations of hepatic ILC1s. *Sci. Immunol.* 7:eabo6641.

Srinivas, S., T. Watanabe, C.-S. Lin, C.M. William, Y. Tanabe, T.M. Jessell, and F. Costantini. 2001. Cre reporter strains produced by targeted insertion of EYFP and ECFP into the ROSA26 locus. *BMC Dev. Biol.* 1:4.

Stark, R., T.H. Wesselink, F.M. Behr, N.A.M. Kragten, R. Arens, F. Koch-Nolte, K.P.J.M. van Gisbergen, and R.A.W. van Lier. 2018. TRM maintenance is regulated by tissue damage via P2RX7. *Sci. Immunol.* 3:eaau1022.

Stokic-Trtica, V., A. Diefenbach, and C.S.N. Klose. 2020. NK Cell Development in Times of Innate Lymphoid Cell Diversity. *Front Immunol* 11:813.

Vivier, E., D. Artis, M. Colonna, A. Diefenbach, J.P. Di Santo, G. Eberl, S. Koyasu, R.M. Locksley, A.N.J. Mckenzie, R.E. Mebius, F. Powrie, and H. Spits. 2018. Innate lymphoid cells: 10 years on. *Cell* 174:1054-1066.

785 Wang, X., H. Peng, J. Cong, X. Wang, Z. Lian, H. Wei, R. Sun, and Z. Tian. 2018. Memory
786 formation and long-term maintenance of IL-7Rα^{+} ILC1s via a lymph node-liver axis.
787 *Nat. Commun.* 9:4854.

788 Weizman, O.E., N.M. Adams, I.S. Schuster, C. Krishna, Y. Pritykin, C. Lau, M.A. Degli-
789 Esposti, C.S. Leslie, J.C. Sun, and T.E. O'Sullivan. 2017. ILC1 confer early host
790 protection at initial sites of viral infection. *Cell* 171:795-808.e712.

791 Weizman, O.E., E. Song, N.M. Adams, A.D. Hildreth, L. Riggan, C. Krishna, O.A. Aguilar,
792 C.S. Leslie, J.R. Carlyle, J.C. Sun, and T.E. O'Sullivan. 2019. Mouse
793 cytomegalovirus-experienced ILC1s acquire a memory response dependent on the
794 viral glycoprotein m12. *Nat. Immunol.* 20:1004-1011.

795 Yomogida, K., T.M. Bigley, T. Trsan, S. Gilfillan, M. Cella, W.M. Yokoyama, T. Egawa, and
796 M. Colonna. 2021. Hobit confers tissue-dependent programs to type 1 innate lymphoid
797 cells. *Proc. Natl. Acad. Sci. USA.* 118:e2117965118.

798 Yu, Y., J.C.H. Tsang, C. Wang, S. Clare, J. Wang, X. Chen, C. Brandt, L. Kane, L.S. Campos,
799 L. Lu, G.T. Belz, A.N.J. Mckenzie, S.A. Teichmann, G. Dougan, and P. Liu. 2016.
800 Single-cell RNA-seq identifies a PD-1^{hi} ILC progenitor and defines its development
801 pathway. *Nature* 539:102-106.

802 Zhou, Y., B. Zhou, L. Pache, M. Chang, A.H. Khodabakhshi, O. Tanaseichuk, C. Benner, and
803 S.K. Chanda. 2019. Metascape provides a biologist-oriented resource for the analysis
804 of systems-level datasets. *Nat. Commun.* 10:1523.
805

Figures

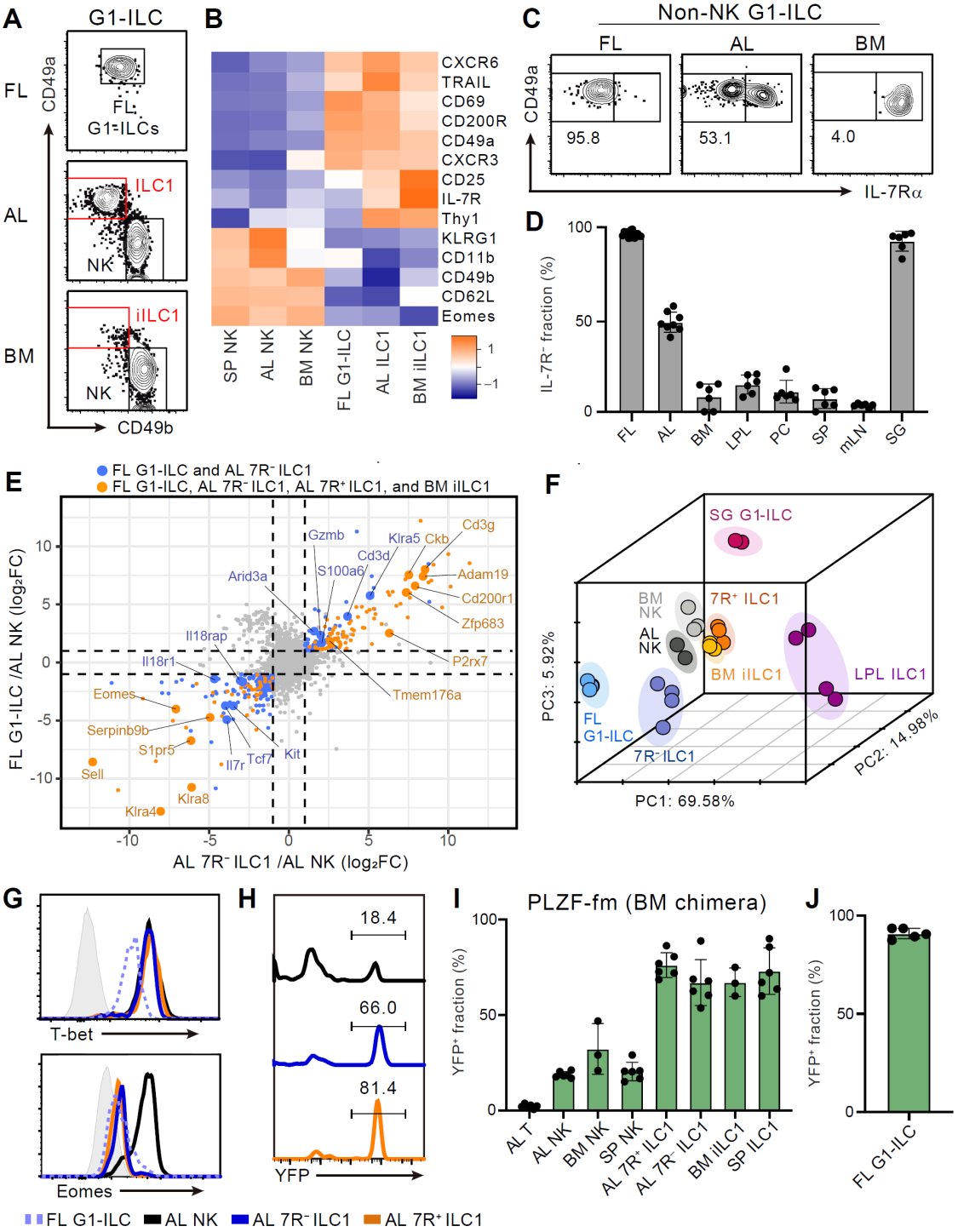

Figure 1. Fetal and adult liver contain *bona fide* ILC1s lacking IL-7R.

(A) Gating strategy of subpopulations of G1-ILCs ($CD3^{-}NK1.1^{+}NKp46^{+}$) in the E18.5 fetal liver (FL), adult liver (AL), and bone marrow (BM). iILC1, immature ILC1.

(B) Heatmap representing log2 transformed mean fluorescence intensity (MFI) of indicated protein expression normalized by z-score transformations. SP, spleen.

(C) Expression of IL-7Rα on G1-ILCs except for CD49a^{-}CD49b^{+} NK cells (non-NK G1-ILCs) in FL, AL, and BM.

(D) The percentages of IL-7R^{-} fractions in non-NK G1-ILCs in the indicated tissues (n = 6–8). LPL, small intestinal lamina propria lymphocytes; PC, peritoneal cavity; mLN, mesenteric lymph node; SG, salivary gland.

(E) Scatter plot showing relative gene expression of FL G1-ILCs and AL 7R^{-} ILC1s compared to AL NK cells in RNA-seq. Genes differentially expressed by FL G1-ILCs, AL 7R^{-} ILC1s, AL 7R^{+} ILC1s, and BM iILC1s (orange) or only by FL G1-ILCs and AL 7R^{-} ILC1s (blue) compared to AL NK cells are highlighted. FC, fold change.

(F) First three principal components in PCA of top 3,000 variant genes.

(G) Expression of T-bet (upper) and Eomes (lower) on FL G1-ILCs as well as NK cells, 7R^{-} ILC1s, and 7R^{+} ILC1s in AL. Shaded histograms (grey) indicate isotype controls.

(H and I) Fate-mapping analysis of adult chimeric mice reconstituted with BM YFP^{-}Lin^{-}Sca1^{+}c-Kit^{+} (LSK) cells from PLZF-GFP-Cre Rosa26-YFP (PLZF-fm) mice. Representative histograms of YFP expression (H) and the percentages of YFP^{+} cells in indicated cell populations (I) are shown (n = 3–6).

(J) The percentage of YFP^{+} cells in FL G1-ILCs in E18.5 straight PLZF-fm mice (n = 5).

Data represent at least two independent experiments (A, C, G, and H), are from three to six biological replicates (B), or are pooled from one (J) or multiple (D and I) independent experiments. RNA-seq data are from two (AL NK cells and SG G1-ILCs), three (AL 7R^{+} ILC1s, BM iILC1s, and BM NK cells), and four (FL G1-ILCs, AL 7R^{-} ILC1s, and LPL ILC1s) biological replicates (E and F). Data are presented as mean ± SD.

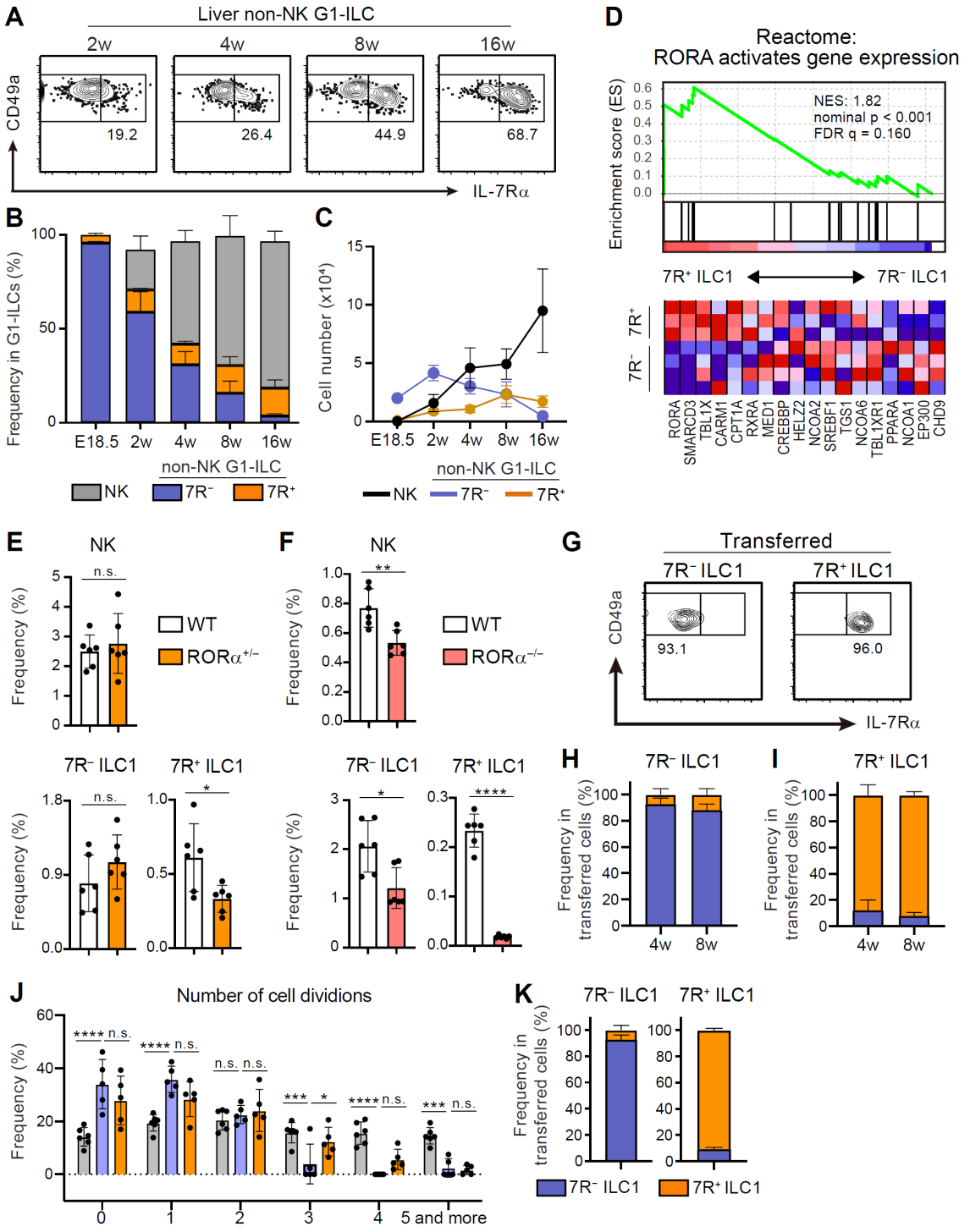

Figure 2. 7R$^+$ ILC1s are dispensable for the development of 7R$^-$ ILC1s in AL.

(A–C) Kinetics of IL-7Rα expression on liver non-NK G1-ILCs with age. Representative FCM profiles (A), the percentages within G1-ILCs (B), and the cell number (C) are shown (*n* = 5–11 for each timepoint).

(D) GSEA of transcriptomes in 7R$^+$ ILC1s compared to 7R$^-$ ILC1s. Eighteen genes included in an indicated gene set from Reactome Pathway are shown. The lower heatmap shows

841 relative gene expression levels in AL $7R^-$ and $7R^+$ ILC1s.
842 (E) The percentages of AL G1-ILC populations in control or ROR$\alpha^{+/-}$ mice (n = 6).
843 (F) The percentages of AL G1-ILC populations in control or ROR$\alpha^{-/-}$ mice (n = 6).
844 (G–I) Flow cytometric (FCM) analysis of transferred AL $7R^-$ and $7R^+$ ILC1s detected in the
845 host liver at 4 weeks and 8 weeks post-transfer. Representative FCM profiles (G) and the
846 percentages of the fate of transferred $7R^-$ ILC1s (H) and $7R^+$ ILC1s (I) are shown (n = 3–6).
847 (J) Host mice received with CPD-eFluor 450-labeled $7R^-$ and $7R^+$ ILC1s are repeatedly
848 stimulated with i.p. injection of IL-15/IL-15Rα complex. The number of transferred cell
849 division based on the FCM analysis of CPD-eFluor 450 dye dilution (n = 5–6) are shown.
850 (K) The percentages of the fate of transferred AL $7R^-$ ILC1s and $7R^+$ ILC1s detected in the
851 liver of host mice injected with IL-15/IL-15Rα complex (n = 5–6).
852 Data are from three (AL $7R^+$ ILC1s) and four (AL $7R^-$ ILC1s) biological replicates (D),
853 represent at least two independent experiments (A and G), or are pooled from one (F) and
854 multiple (B, C, E, H–K) independent experiments. Data are presented as mean ± SD. *p <
855 0.05, **p < 0.01, ***p < 0.001, ****p < 0.0001.
856

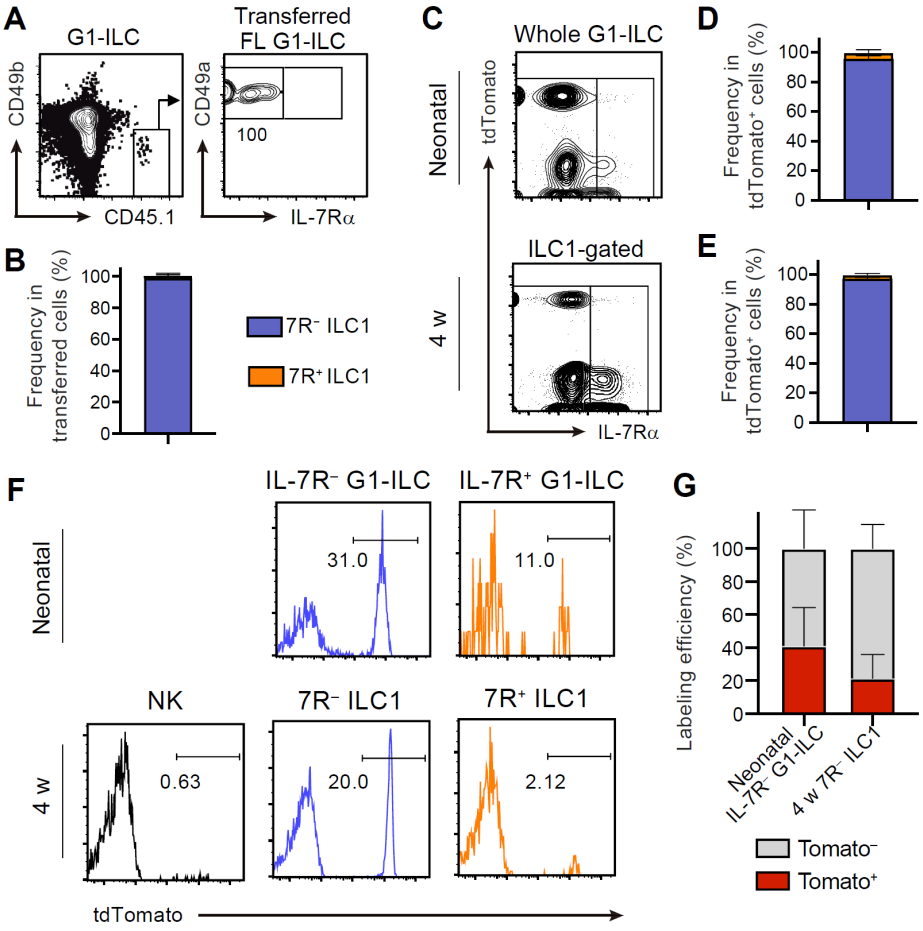

857 **Figure 3. FL G1-ILCs exclusively give rise to 7R$^-$ ILC1s.**

858 (A and B) FCM analysis of transferred FL G1-ILCs (CD45.1) detected in the host liver
859 (CD45.2) at 4 weeks post-transfer. Representative FCM profiles (A) and the percentages of
860 transferred cell fate (B) are shown (n = 4).

861 (C–E) FCM analysis of tdTomato$^+$ cells in neonatal and adult NKp46-CreERT2 Rosa26-
862 tdTomato mice treated with tamoxifen at E17.5. Representative FCM plots (C) and the
863 percentage of the fate of tdTomato$^+$ cells in neonates (D; n = 10) and 4 weeks old mice (E; n
864 = 5) are shown. Blue, IL-7R$^-$ fraction; orange, IL-7R$^+$ fraction.

865 (F and G) FCM analysis of tdTomato expression on indicated G1-ILC populations in NKp46-
866 Cre Rosa26-tdTomato mice treated with tamoxifen at E17.5. Representative histograms (F)
867 and the percentages of tdTomato$^+$ and tdTomato$^-$ fractions in neonatal IL-7R$^-$ G1-ILCs and
868 7R$^-$ ILC1s in 4 weeks old mice (G) are shown (n = 5–10).

869 Data represent at least two independent experiments (A, C, and F). Data are pooled from
870 multiple independent experiments (B, D, E, and G) and presented as mean ± SD.

871

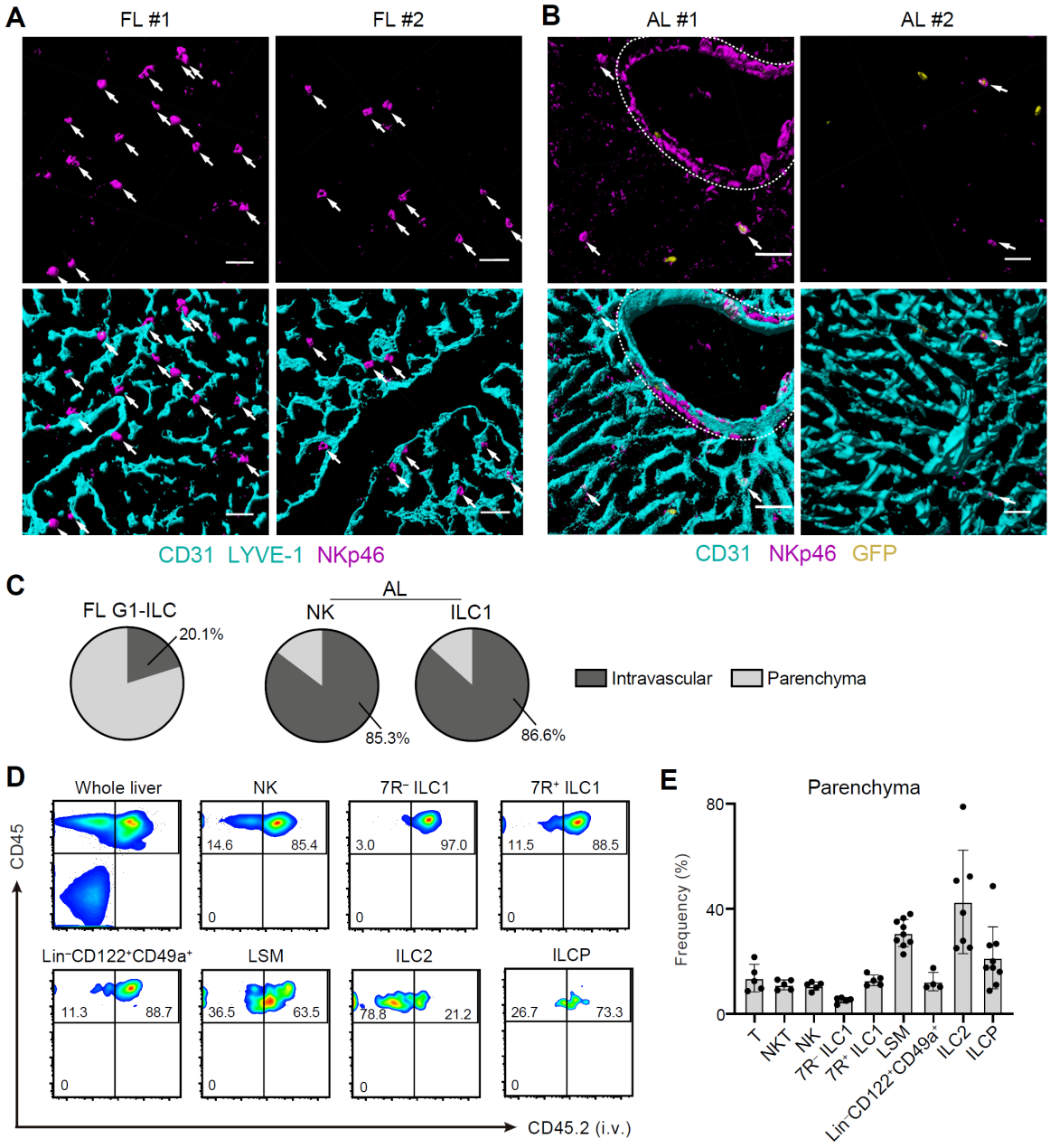

872 **Figure 4. Liver G1-ILCs shift distributions from parenchyma to sinusoids during**
873 **development.**

874 (A and B) 3D-reconstructed immunofluorescence images of frozen sections of FL from WT
875 mice (A) and AL from CXCR6$^{GFP/+}$ mice (B) stained with anti-NKp46 (magenta) and anti-
876 CD31 and/or anti-LYVE-1 (for FL endothelium) (cyan) antibodies. GFP signals are shown in
877 yellow. White arrows indicate G1-ILCs. Hepatic artery is circled by a dotted line. Scale bar,
878 40 μm.

879 (C) The percentages of indicated G1-ILC subsets localized inside (intravascular) or outside
880 (parenchyma) of the blood vessels. Data represent randomly counted 169 cells for FL G1-
881 ILCs pooled from four E18.5 WT mice and 232 cells for AL NK cells as well as 136 cells for

AL ILC1s pooled from four CXCR6$^{GFP/+}$ mice.

(D and E) FCM analysis of AL of mice injected i.v. with PE/Cy7 anti-CD45.2 antibody 2 min before the liver perfusion and leukocyte isolation. Representative FCM profiles (D) and the percentages of cells unlabeled by i.v. CD45.2 staining within CD45$^+$ cells (considered as parenchyma-distributed cells) (E) are shown (n = 4–9).

Data represent four mice (A and B) or at least two independent experiments (D). Data are pooled from multiple independent experiments (C and E) and presented as mean ± SD.

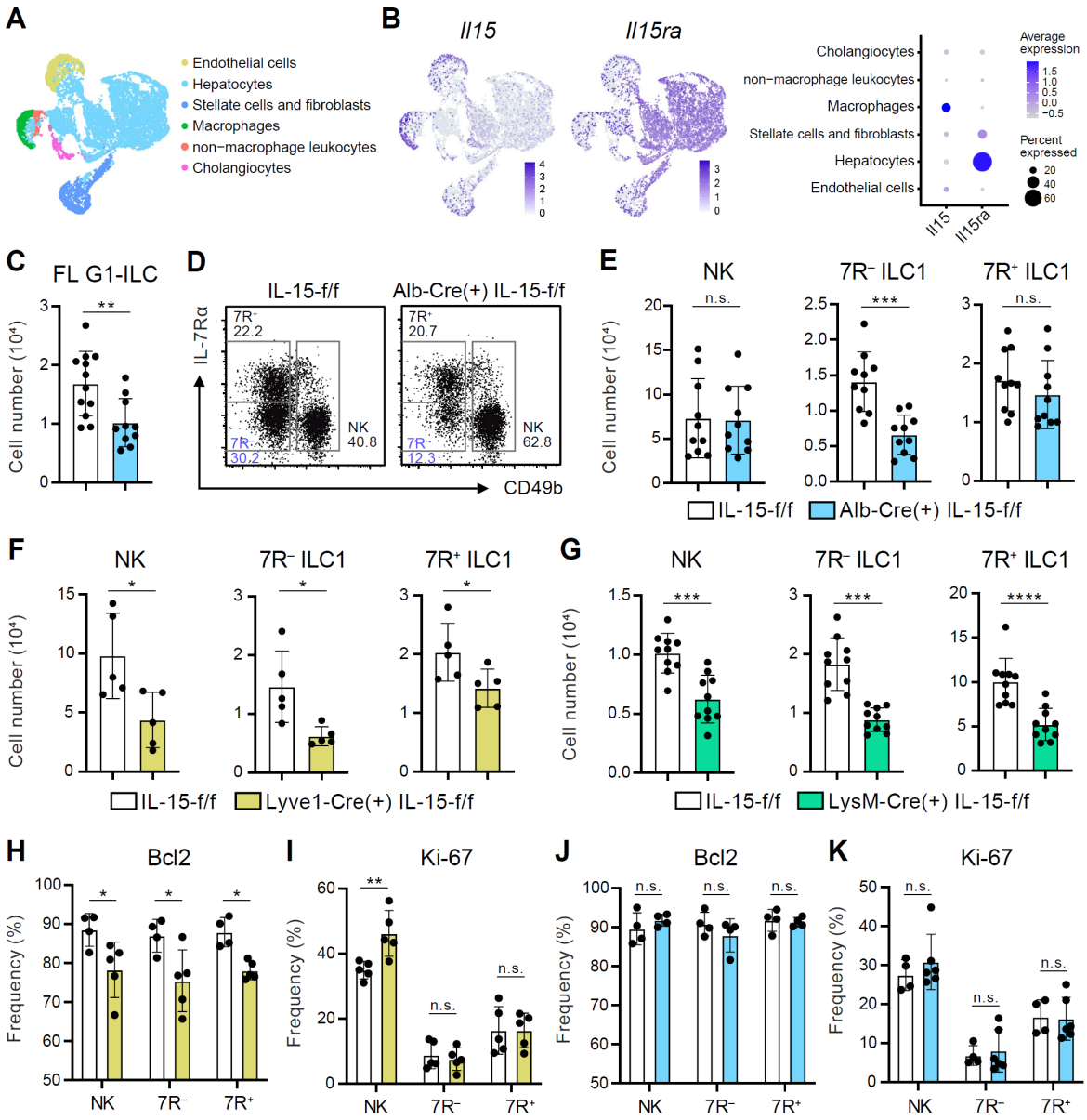

890 **Figure 5. Hepatocytes provide the parenchymal IL-15 niche regulating the local**
891 **development of 7R⁻ ILC1s.**

892 (A and B) Single nuclei RNA-seq (snRNA-seq) analysis of mouse whole liver cells (Liver
893 Cell Atlas; www.livercellatlas.org). UMAP visualization (A) and expression levels of *Il15*
894 and *Il15ra* (B) in each cell population assigned in Figure 5–figure supplement 1B are shown.
895 (C) The cell number of FL G1-ILCs in control or IL-15$^{Alb\text{-}Cre}$ mice (n = 10–12).
896 (D and E) FCM analysis of AL G1-ILCs in control or IL-15$^{Alb\text{-}Cre}$ mice. Representative FCM
897 plots (D) and the cell number of each population (E) are shown (n = 10).
898 (F and G) The cell number of indicated G1-ILC populations in IL-15$^{Lyve1\text{-}Cre}$ mice (F; n = 5)
899 or IL-15$^{LysM\text{-}Cre}$ mice (G; n = 10) compared to controls.
900 (H and I) The percentages of Bcl-2 (H; n = 4–5) and Ki-67 (I; n = 5) expressing cells within

each G1-ILC population in control or IL-15$^{Lyve1\text{-}Cre}$ mice.

(J and K) The percentages of Bcl-2 (J; $n = 4$) and Ki-67 (K; $n = 4–6$) expressing cells within each G1-ILC population in control or IL-15$^{Alb\text{-}Cre}$ mice.

Data represent three independent experiments (D) or are pooled from multiple independent experiments (C and E–K) and presented as mean ± SD. $^{*}p < 0.05$, $^{**}p < 0.01$, $^{***}p < 0.001$, $^{****}p < 0.0001$.

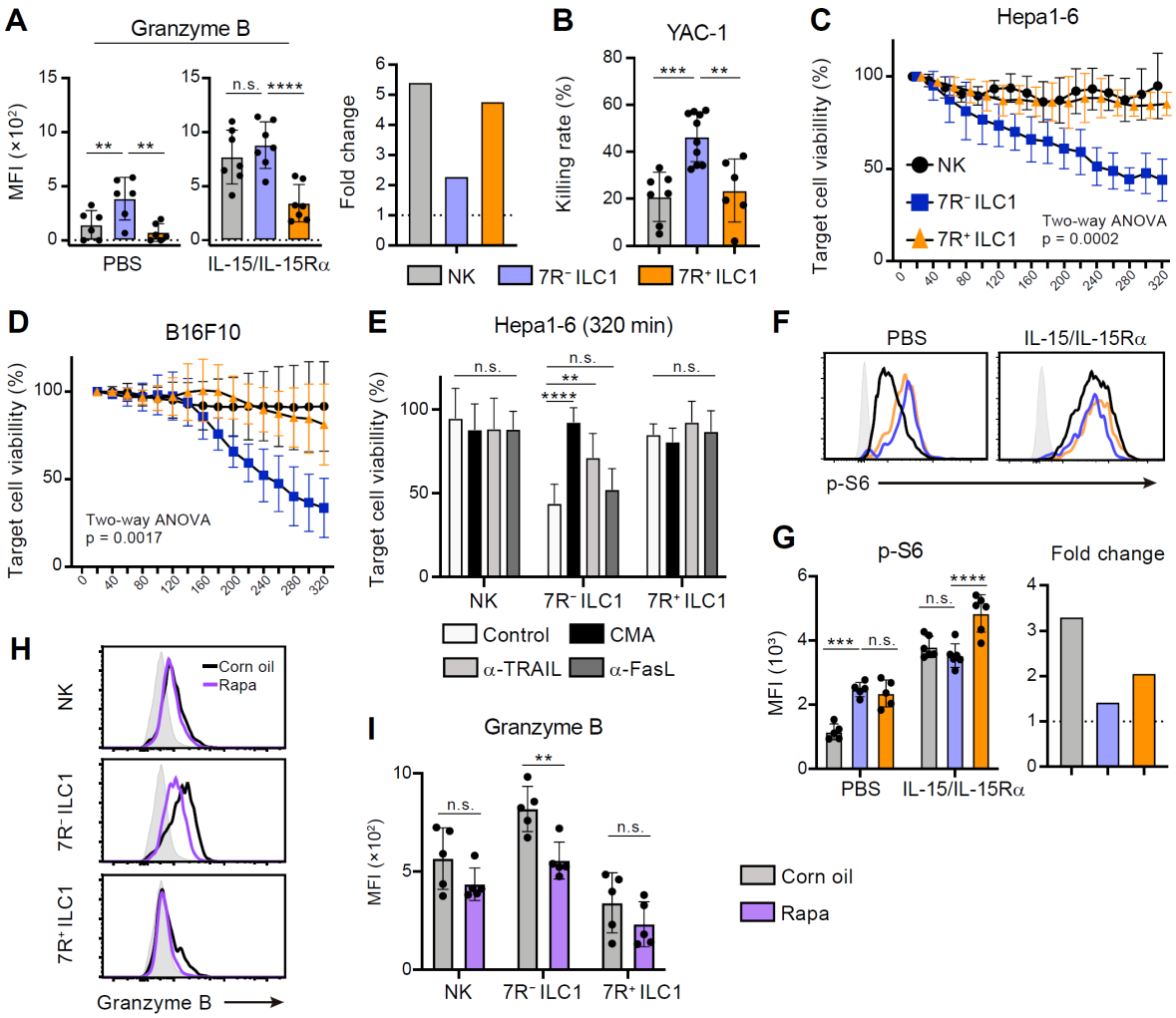

908 **Figure 6. 7R⁻ ILC1s exhibit cytotoxicity via granzyme B expression underpinned by**
909 **steady-state mTOR activation.**

910 (A) Granzyme B expression on each AL G1-ILC population in control or IL-15/IL-15Rα-
911 treated mice. MFI (left) and its fold change after the IL-15/IL-15Rα treatments (right) are
912 shown (n = 6–7).

913 (B) The percentages of annexin V^+PI^+ YAC-1 cells in flow-based cytotoxicity assays. Freshly
914 isolated effector cells were co-cultured with target cells for 4 hours (E:T ratio = 10:1) (n = 6–
915 10).

916 (C and D) Target cell viability at each timepoint in time-lapse cytotoxicity assay using Hepa1-
917 6 cells (C; n = 6) and B16F10 cells (D; n = 7–8) as target cells. Freshly isolated effector cells
918 were co-cultured with target cells up to 6 hours (E:T ratio = 10:1).

919 (E) Hepa1-6 cell viability at 320 min in time-lapse cytotoxicity assays supplemented with
920 concanamycin A (CMA) or neutralizing antibody for TRAIL (α-TRAIL) or FasL (α-FasL)
921 compared to vehicle-supplemented controls (n = 6).

(F and G) FCM analysis of phosphorylation of S6 in NK cells (black), $7R^-$ ILC1s (blue), and $7R^+$ ILC1s (orange) in control or IL-15/IL-15Rα-treated mice. Representative histograms (F) and MFI (left) and its fold change after the IL-15/IL-15Rα treatments (right) (G) are shown (n = 5–6). Shaded histograms (grey) indicate isotype controls.

(H and I) FCM analysis of granzyme B expressed on each AL G1-ILC population in control or rapamycin-treated mice. Representative histograms (H) and MFI (I) are shown (n = 5). Shaded histograms (grey) indicate isotype controls.

Data represent at least two independent experiments (F and H) or are pooled from multiple independent experiments (A–E, G, and I) and are presented as mean ± SD. $^{**}p < 0.01$, $^{***}p < 0.001$, $^{****}p < 0.0001$.

Figure Supplements

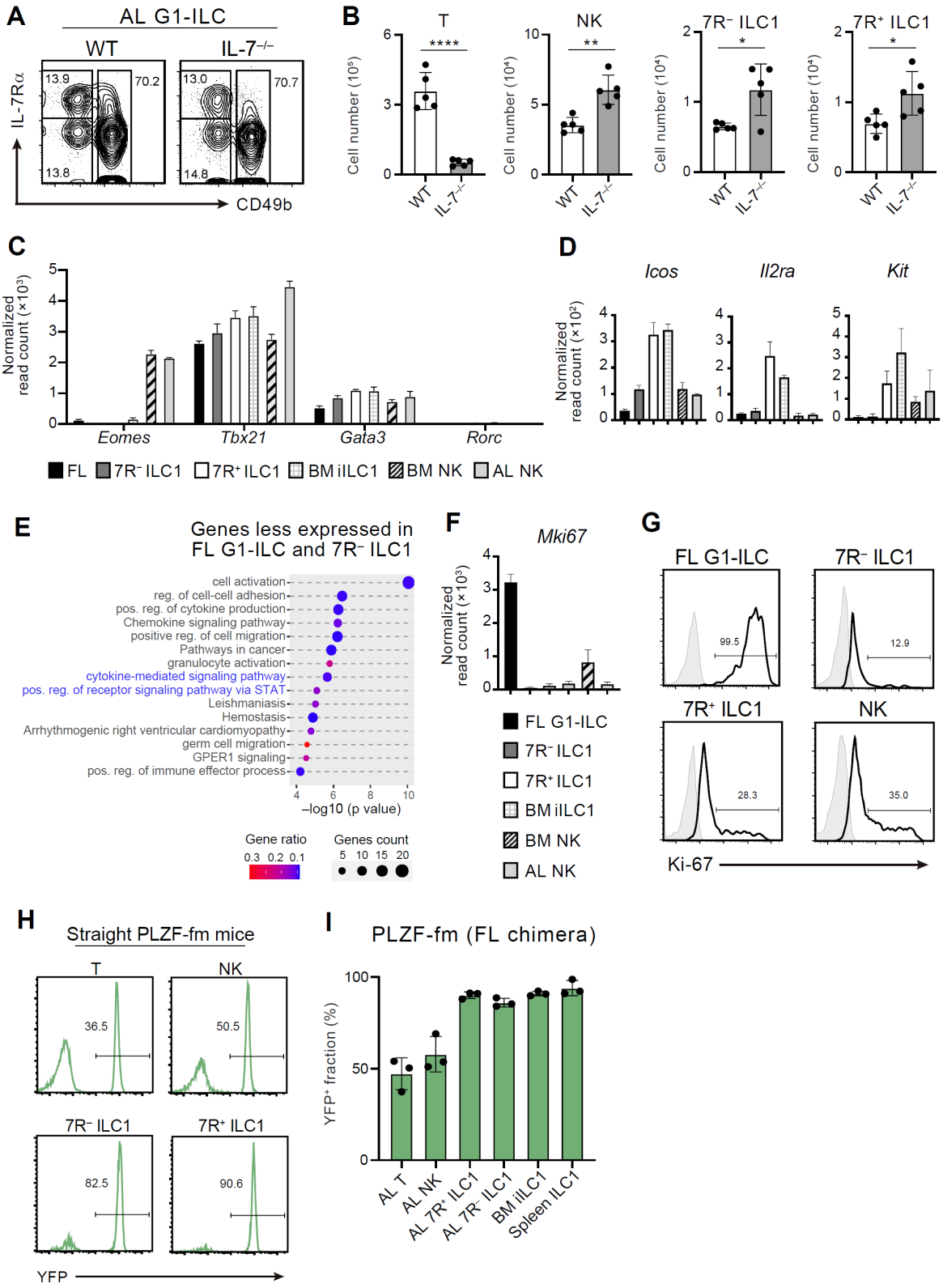

Figure 1–figure supplement 1. Characterization of fetal and adult G1-ILC identities.

(A and B) Flow cytometry (FCM) analysis of AL lymphocytes in control or IL-7$^{-/-}$ mice.

937 Representative FCM profiles of G1-ILCs (A) and the cell number of each cell population (B)
938 are shown (n = 5).
939 (C) Normalized read counts of *Eomes*, *Tbx21*, *Gata3*, and *Rorc* expressed on each G1-ILC
940 population in FL, AL, and BM obtained from RNA-seq.
941 (D) Normalized read counts of *Icos*, *Il2ra*, and *Kit* expressed on each G1-ILC population.
942 (E) Dot plots showing the significantly enriched pathways on DEGs less expressed in FL G1-
943 ILCs and 7R$^-$ ILC1s but not in 7R$^+$ ILC1s and BM iILC1s compared to AL NK cells,
944 analyzed by Metascape. Gene ratio indicates the ratio of the gene number corresponding to
945 the DEGs in the pathway (gene count) to the total gene number in the pathway. Pathways
946 related to cytokine responses were highlighted (blue).
947 (F) Normalized read counts of *Mki67* expressed on each G1-ILC population obtained from
948 RNA-seq.
949 (G) Expression of Ki-67 protein on FL G1-ILCs as well as NK cells, 7R$^-$ ILC1s, and 7R$^+$
950 ILC1s in AL.
951 (H) Representative histograms of YFP expression in AL lymphocyte populations of straight
952 PLZF-GFP-Cre Rosa26-YFP (PLZF-fm) mice (n = 2).
953 (I) Fate-mapping analysis of adult chimeric mice reconstituted with FL YFP$^-$ LSK cells from
954 PLZF-fm mice. The percentages of YFP$^+$ cells in indicated cell populations are shown (n = 3).
955 Data are from two (AL NK cells), three (AL 7R$^+$ ILC1s, BM iILC1s, and BM NK cells), and
956 four (FL G1-ILCs and AL 7R$^-$ ILC1s) biological replicates (C–F). Data represent one (H and
957 I) or two (A and G) independent experiments or pooled from multiple independent
958 experiments (B). Data are presented as mean ± SD. *$p < 0.05$, **$p < 0.01$, ****$p < 0.0001$.
959

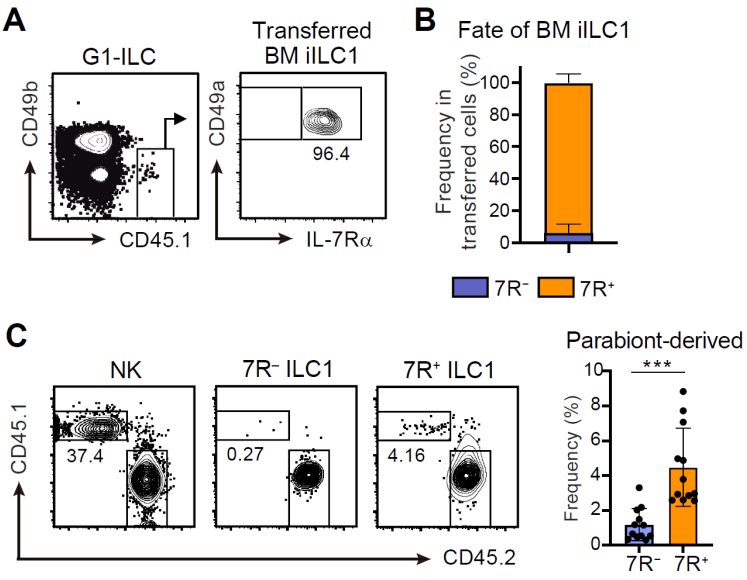

960 **Figure 2–figure supplement 1. BM iILC1s have ability to give rise to AL 7R$^+$ ILC1s *in***
961 ***vivo*.**

962 (A and B) FCM analysis of transferred BM iILC1s (CD45.1) detected in the host liver
963 (CD45.2) at 4 weeks post-transfer. Representative FCM profiles (A) and the percentages of
964 transferred cell fate (B) are shown (n = 6).

965 (C) FCM analysis of AL G1-ILCs in CD45.2 WT mice conjoined with CD45.1 WT mice in
966 parabiosis experiments. Representative FCM profiles and the percentages of parabiont-
967 derived cells in AL 7R$^-$ and 7R$^+$ ILC1s are shown (n = 12).

968 Data represent at least two independent experiments (A and C), or are pooled from multiple
969 independent experiments (B and C). Data are presented as mean ± SD. ***$p < 0.001$.

970

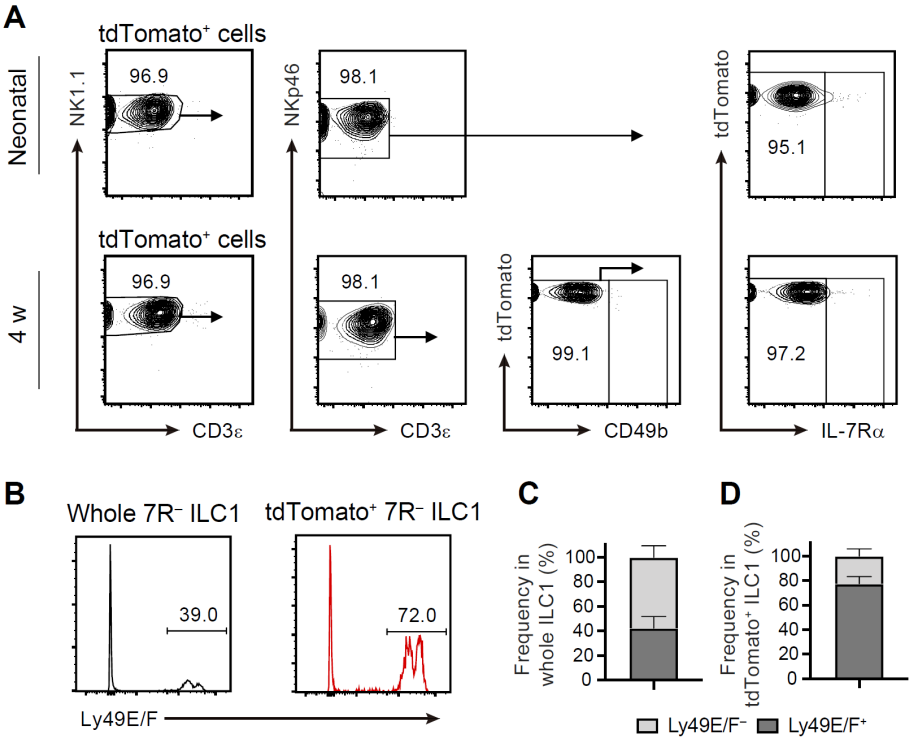

971 **Figure 3–figure supplement 1. FL G1-ILCs contribute to AL 7R⁻ ILC1 pool.**

972 (A) FCM analysis of tdTomato$^+$ cells in AL of NKp46-CreERT2 Rosa26-tdTomato mice
973 treated with tamoxifen at E17.5. Representative FCM plots in neonates (n = 10) and 4 weeks
974 old mice (n = 5) are shown.

975 (B–D) FCM analysis of Ly-49E/F expression on 7R$^-$ ILC1s. Representative histograms (D)
976 and the percentages of Ly-49E/F$^+$ and Ly-49E/F$^-$ fraction in whole 7R$^-$ ILC1s (C) or in
977 tdTomato$^+$ 7R$^-$ ILC1s (D) are shown (n = 5).

978 Data represent at least two independent experiments (A and B) or are pooled from multiple
979 independent experiments (C and D). Data are presented as mean ± SD.

980

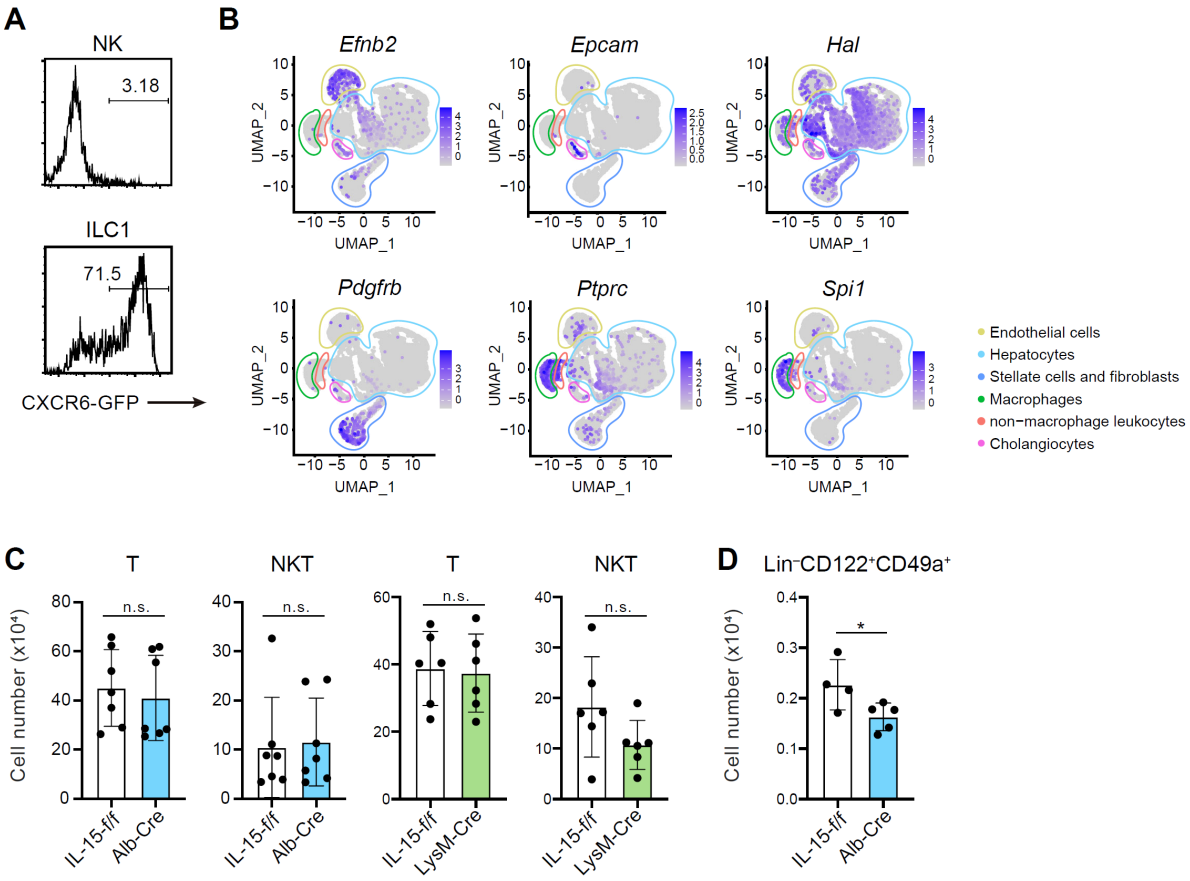

981 **Figure 5–figure supplement 1. Liver IL-15-producing cells supports lymphoid cells in a**
982 **subset-dependent manner.**

983 (A) Expression of GFP on AL NK cells and ILC1s in CXCR6$^{GFP/+}$ mice.

984 (B) UMAP visualization of snRNA-seq analysis of mouse whole liver cells (Liver Cell Atlas;

985 www.livercellatlas.org). Cell identity of each cluster was defined based on the expression of

986 *Efnb2*, *Epcam*, *Hal*, *Pdgfb*, *Ptprc*, and *Spi1*.

987 (C) The cell number of AL T cells and CD3^{+}NK1.1^{+} (NKT) cells in control, IL-15$^{Alb-Cre}$ mice,

988 or IL-15$^{LysM-Cre}$ mice (n = 6–7).

989 (D) The cell number of Lin^{-}CD122^{+}CD49a^{+} cells in control or IL-15$^{Alb-Cre}$ mice (n = 4–5).

990 Data represent two independent experiments (A) or are pooled from multiple independent

991 experiments (C and D) and presented as mean ± SD. *$p < 0.05$.

992

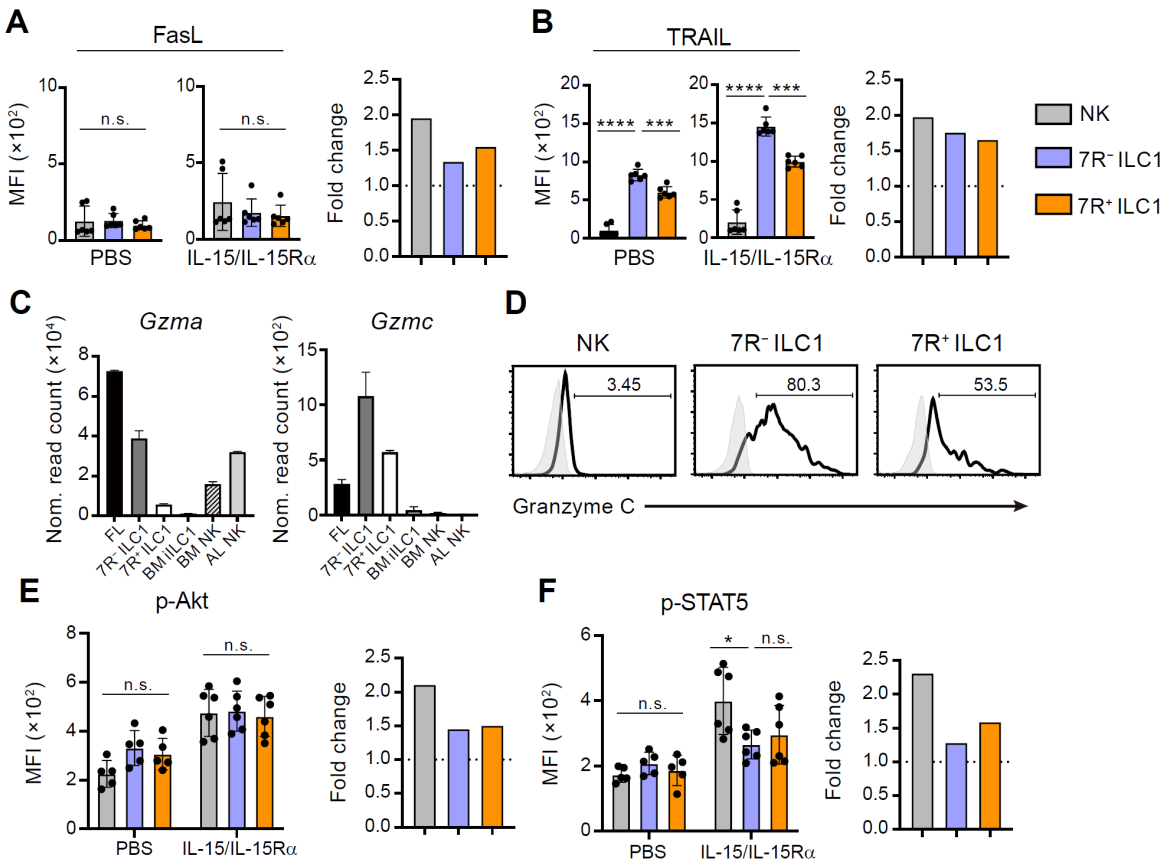

993 **Figure 6–figure supplement 1. Differential effector molecule expression and cytokine**
994 **responsiveness among heterogenous G1-ILC subsets.**

995 (A and B) Expression of FasL (A) and TRAIL (B) on each AL G1-ILC population in control
996 or IL-15/IL-15Rα-treated mice (n = 6). MFI (left) and its fold change after the IL-15/IL-
997 15Rα treatments (right) are shown.

998 (C) Normalized read counts of *Gzma* and *Gzmc* expressed on each G1-ILC population
999 obtained from RNA-seq.

1000 (D) Expression of granzyme C protein on NK cells, 7R$^-$ ILC1s, and 7R$^+$ ILC1s in AL.

1001 (E and F) Phosphorylation levels of Akt (E) and STAT5 (F) on each AL G1-ILC population in
1002 control or IL-15/IL-15Rα-treated mice (n = 5–6). MFI (left) and its fold change after the IL-
1003 15/IL-15Rα treatments (right) are shown.

1004 Data are from two (AL NK cells), three (AL 7R$^+$ ILC1s, BM iILC1s, and BM NK cells), and
1005 four (FL G1-ILCs and AL 7R$^-$ ILC1s) biological replicates (C). Data represent two
1006 independent experiments (D) or are pooled from multiple independent experiments (A, B, E,
1007 and F) and presented as mean ± SD. *$p < 0.05$, ***$p < 0.001$, ****$p < 0.0001$.

1008